JOURNAL OF Applied Polymer SCIENCE

Modeling and simulation of fiber-reinforced polymer mold-filling with phase change

Fang Wang, Junlin Li, Binxin Yang
Department of Mathematics, Taiyuan University of Science and Technology, Taiyuan 030024, People's Republic of China
Correspondence to: J. L. Li (E-mail: lijunlin9726@163.com)

ABSTRACT: A gas-solid-liquid three-phase model for the simulation of fiber-reinforced composites mold-filling with phase change is established. The influence of fluid flow on the fibers is described by Newton's law of motion, and the influence of fibers on fluid flow is described by the momentum exchange source term in the model. A revised enthalpy method that can be used for both the melt and air in the mold cavity is proposed to describe the phase change during the mold-filling. The finite-volume method on a non-staggered grid coupled with a level set method for viscoelastic-Newtonian fluid flow is used to solve the model. The "frozen skin" layers are simulated successfully. Information regarding the fiber transformation and orientation is obtained in the mold-filling process. The results show that fibers in the cavity are divided into five layers during the mold-filling process, which is in accordance with experimental studies. Fibers have disturbance on these physical quantities, and the disturbance increases as the slenderness ratio increases. During mold-filling process with two injection inlets, fiber orientation around the weld line area is in accordance with the experimental results. At the same time, single fiber's trajectory in the cavity, and physical quantities such as velocity, pressure, temperature, and stresses distributions in the cavity at end of mold-filling process are also obtained. © 2015 Wiley Periodicals, Inc. J. Appl. Polym. Sci. **2016**, *133*, 42881.

KEYWORDS: fibers; surfaces and interfaces; theory and modeling

Received 29 June 2015; accepted 27 August 2015
DOI: 10.1002/app.42881

INTRODUCTION

Mold-filling is the main stage of injection molding and is a notably complex physical process. In this process, under the action of pressure, a non-Newtonian polymer melt at elevated temperature is injected into the mold cavity, which is at a lower temperature. However, the temperature difference between the melt and the mold cavity leads to solidification, volume shrinkage and possible crystallisation. Therefore, the quality of injection-molded parts is very difficult to predict and control without simulations relying on complex computer techniques. Some researchers have studied the mold-filling process numerically, using tools ranging from the Hele-Shaw model to the Navier-Stokes equations, without considering the interface motion.[1–10] Some studies investigating the mold-filling process using interface tracking techniques have been published.[11–21] However, these papers studied the mold-filling problem by ignoring the temperature variation despite the temperature on the side walls of the mold cavity being much lower than that of the melt. As a result, near the mold walls, the viscosity is higher due to the decreased temperature. The polymer tends to solidify as the viscosity increases, which is known as a phase change or a "frozen skin" layer. Meanwhile, a great amount of heat, known as latent heat, is released at the moment when the melt begins to solidify, which stops the melt from solidifying. Because the frozen skin layer is not desirable, as it contributes to the "molded-in" strains in the molded article, the phase change and the temperature variation should be studied carefully. However, few studies have considered the phase change and latent heat in the mold-filling process.

However, fibers motion and orientation must be considered for fiber-reinforced composites mold-filling process. However, many papers focus more on the mechanical properties of fiber-reinforced composites than the forming process of fiber-reinforced composites.[22–24] The fiber orientation in the mold-filling process was simulated in some articles.[25–29] However, such articles as dynamic simulations of the mold-filling process for fiber-reinforced composites are few. The difficulty lies in the fact that both fiber transformation and orientation and interface evolution must be considered simultaneously. Yang *et al.*[30] proposed a viscoelastic-Newtonian model for the mold-filling process, in which the dynamic behaviors and the interface of fiber-reinforced composites during the mold-filling process can be captured at each time step. However, the mold-filling process was isothermal, and phase changes were not considered in their article.

© 2015 Wiley Periodicals, Inc.

Table I. Definition of the Constants and Functions in the Constitutive Equation[36]

Equation		m	ψ	Λ	S_ψ
τ_{xx}	normal stress	Wi	τ_{xx}	0	$2(1-\beta)\frac{\partial u}{\partial x}+2Wi\tau_{xx}\frac{\partial u}{\partial x}+2Wi\tau_{xy}\frac{\partial u}{\partial y}-f(\lambda,\boldsymbol{\tau})\tau_{xx}$ $-[f(\lambda,\boldsymbol{\tau})-1]\frac{1-\beta}{Wi}-\alpha\frac{Wi}{1-\beta}(\tau_{xx}^2+\tau_{xy}^2)$
τ_{xy}	shear stress	Wi	τ_{xy}	0	$(1-\beta)\left(\frac{\partial v}{\partial x}+\frac{\partial u}{\partial y}\right)+Wi\tau_{xx}\frac{\partial v}{\partial x}+Wi\tau_{yy}\frac{\partial u}{\partial y}$ $-f(\lambda,\boldsymbol{\tau})\tau_{xy}-\alpha\frac{Wi}{1-\beta}\tau_{xy}(\tau_{xx}+\tau_{yy})$
τ_{yy}	normal stress	Wi	τ_{yy}	0	$2(1-\beta)\frac{\partial v}{\partial y}+2Wi\tau_{yy}\frac{\partial v}{\partial y}+2Wi\tau_{xy}\frac{\partial v}{\partial x}-f(\lambda,\boldsymbol{\tau})\tau_{yy}$ $-[f(\lambda,\boldsymbol{\tau})-1]\frac{1-\beta}{Wi}-\alpha\frac{Wi}{1-\beta}(\tau_{yy}^2+\tau_{xy}^2)$
τ_{zz}	stress	Wi	τ_{zz}	0	$-f(\lambda,\boldsymbol{\tau})\tau_{zz}-[f(\lambda,\boldsymbol{\tau})-1]\frac{1-\beta}{Wi}-\alpha\frac{Wi}{1-\beta}\tau_{zz}^2$

In this article, a gas-solid-liquid three-phase model for the simulation of the mold-filling process for fiber-reinforced composites with phase change is established. A revised enthalpy method that can be used for both the melt and the air in the mold cavity is proposed to describe the phase change during the mold-filling. The interaction between the fibers and the polymer melt is considered in the model. A finite-volume method using a nonstaggered grid coupled with a level set method for viscoelastic-Newtonian fluid flow is used to solve the model.

The remainder of this articles is organized as follows. In section "Mathematical Model," the mathematical model is presented for the simulation of the mold-filling process. In section "Fiber Dynamics," the equations are given to described fiber translation and orientation during the mold-filling process. In section "Numerical Method," numerical methods are presented to solve the mathematical model in section "Mathematical Model." And numerical tests are taken to test the validity of the methodology. In section "Results and Analysis" simulation results are shown and discussed. In section "Conclusions," some brief conclusions are drawn.

MATHEMATICAL MODEL

Level Set Equation for Interface Evolution

Interface tracking plays an important role in the numerical simulation of mold-filling process. We use the corrected level set method proposed by Sussman *et al.*[31,32] to capture the interface in the article.

The basis of the level set method is indicating the interface implicitly by a level set function $\phi(x,y,t)$, which is defined by the algebraic distance between any point of the domain and the melt flow front. The melt flow front is thus described by the zero level sets of the level set function ϕ. In this article, the following level set equation is chosen[33]

$$\frac{\partial\phi}{\partial t}+\mathbf{u}\cdot\nabla\phi=0 \tag{1}$$

where $\mathbf{u}$ is the velocity vector.

Moreover, a reinitialization algorithm must be applied to keep ϕ as the algebraic distance to the interface. The algorithm is based on the iterative solution of the following initial value problem[33]

$$\begin{cases}\dfrac{\partial\phi}{\partial \mathrm{t_r}}=sign(\phi_0)(1-|\nabla\phi|)\\ \phi(x,0)=\phi_0(x)\end{cases} \tag{2}$$

where t_r is a pseudo time and $\mathrm{sign}(\phi_0)$ is the sign function of ϕ, which is defined as

$$\mathrm{sign}(\phi_0)=\frac{\phi_0}{\sqrt{{\phi_0}^2+[\min(\Delta x,\Delta y)]^2}} \tag{3}$$

where Δx and Δy are the grid widths along the x and y directions, respectively. $[\min(\Delta x,\Delta y)]^2$ is used here to prevent division by zero.

Equation (2) does not change the position of the zero level set of ϕ Unfortunately, in numerical computation, this may not be true. We use the method presented by Sussman *et al.*[31,32] to improve the accuracy of solving the reinitialization equation. A local correction item $\varpi\delta_\varepsilon(\phi)|\nabla\phi|$, is added to the reinitialization eq. (2). Thus, the revised equation is[31,32]

$$\frac{\partial\phi}{\partial t_r}+\mathrm{sign}(\phi_0)(|\nabla\phi|-1)=\varpi\delta_\varepsilon(\phi)|\nabla\phi| \tag{4}$$

where ϖ is a local correction coefficient and the smoothed Dirac delta function $\delta_\varepsilon(\phi)$ is defined as

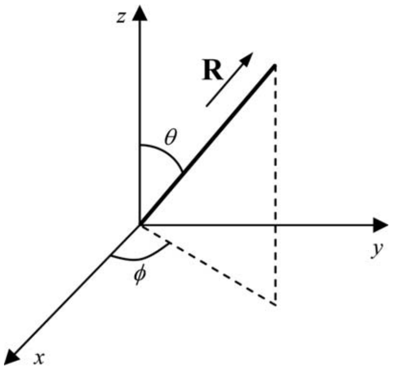

Figure 1. A fiber orientation vector in Cartesian coordinates.

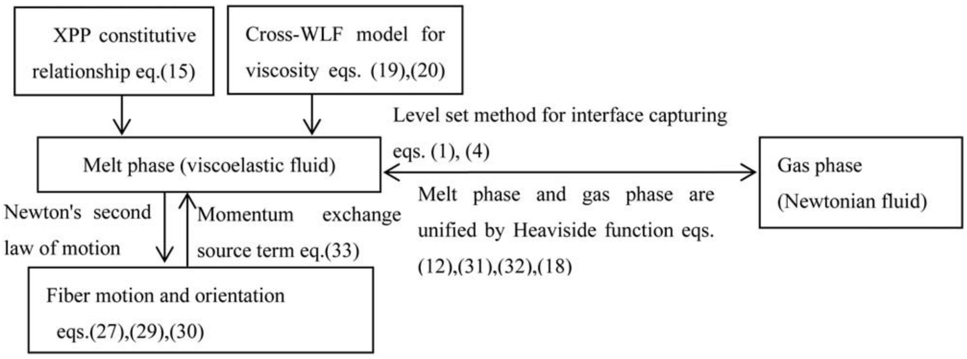

Figure 2. Coupling relationship between equations.

$$\delta_\varepsilon(\phi)=\begin{cases}\dfrac{1}{2\varepsilon}\left(1+\cos\left(\dfrac{\pi\phi}{\varepsilon}\right)\right), & |\phi|<\varepsilon\\ 0, & \text{otherwise}\end{cases} \tag{5}$$

Here, ε is the thickness of the interface, which is proportional to the spatial mesh.

Governing Equations for the Fluid

The fluid problem of this paper to be solved is two-dimension and time-dependent, the computational domain is the vertical middle plane of the mold without taking into account the width W. Both the gas phase and the liquid melt are regarded as incompressible, the gas phase in the cavity is a Newtonian fluid, and the liquid phase in the cavity is a viscoelastic melt. The two phases are treated in a single Eulerian grid by the level set method in this article.

Define the Heaviside function as[31]

$$H_\varepsilon(\phi)=\begin{cases}0 & \phi<-\varepsilon\\ \dfrac{1}{2}\left[1+\dfrac{\phi}{\varepsilon}+\sin\left(\pi\phi/\varepsilon\right)/\pi\right] & |\phi|\le\varepsilon\\ 1 & \phi>\varepsilon\end{cases} \tag{6}$$

The governing equations for the two-phase flow can be written as a united generalized Navier-Stokes system by the Heaviside function, the continuity equation, momentum equations, and energy equations as below[34]

Continuity equation

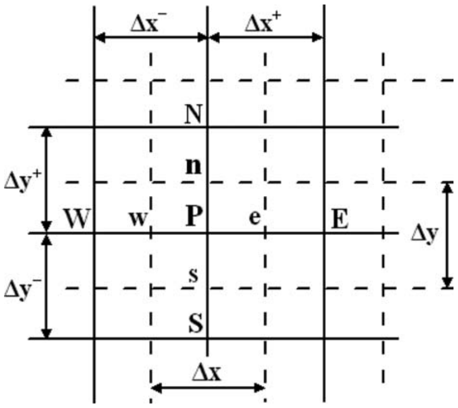

Figure 3. Sketch map of the nonstaggered meshes.

$$\frac{\partial\rho}{\partial t}+\frac{\partial(\rho u)}{\partial x}+\frac{\partial(\rho v)}{\partial y}=0 \tag{7}$$

u-momentum equation

$$\frac{\partial(\rho u)}{\partial t}+\frac{\partial(\rho uu)}{\partial x}+\frac{\partial(\rho vu)}{\partial y}-\left(\frac{\partial^2(\eta u)}{\partial x^2}+\frac{\partial^2(\eta u)}{\partial y^2}\right)$$
$$=-\frac{\partial p}{\partial x}+(\beta-1)\left(\frac{\partial^2(\eta u)}{\partial x^2}+\frac{\partial^2(\eta u)}{\partial y^2}\right)H_\varepsilon(\phi)+\frac{\partial\tau_{xx}}{\partial x}H_\varepsilon(\phi) \tag{8}$$
$$+\frac{\partial\tau_{xy}}{\partial y}H_\varepsilon(\phi)$$

v-momentum equation

$$\frac{\partial(\rho v)}{\partial t}+\frac{\partial(\rho uv)}{\partial x}+\frac{\partial(\rho vv)}{\partial y}-\left(\frac{\partial^2(\eta v)}{\partial x^2}+\frac{\partial^2(\eta v)}{\partial y^2}\right)$$
$$=-\frac{\partial p}{\partial y}+(\beta-1)\left(\frac{\partial^2(\eta v)}{\partial x^2}+\frac{\partial^2(\eta v)}{\partial y^2}\right)H_\varepsilon(\phi)+\frac{\partial\tau_{yx}}{\partial x}H_\varepsilon(\phi) \tag{9}$$
$$+\frac{\partial\tau_{yy}}{\partial y}H_\varepsilon(\phi)$$

Energy equations

$$\frac{\partial}{\partial t}(\rho CT)+\nabla\cdot(\rho C\mathbf{u}T)=\nabla\cdot(K\nabla T)+\boldsymbol{\sigma}:\mathbf{D} \tag{10}$$

Where

$$\rho(\phi)=\rho_g+\left(\rho_m-\rho_g\right)H_\varepsilon(\phi)\ \ \eta(\phi)=\eta_g+\left(\eta_m-\eta_g\right)H_\varepsilon(\phi)$$
$$C(\phi)=C_g+(C_m-C_g)H_\varepsilon(\phi)\ \ K(\phi)=K_g+(K_m-K_g)H_\varepsilon(\phi)$$

ρ is the density; u, v are the x-, y-direction velocity, respectively; η is the viscosity; p is the pressure; β is the ratio of the Newtonian viscosity to the total viscosity; C is the specific heat; T is the temperature; K is the thermal conductivity; $\boldsymbol{\sigma}$ is the Cauchy stress tensor, $\boldsymbol{\sigma}=-p\mathrm{I}+\eta\mathbf{D}$; and the subscripts m and g represent the melt and gas phases, respectively.

Notice that in eq. (7), the density ρ cannot be omitted because the values of ρ may be different on the two sides of the interface.

Because the melt for the mold-filling is viscoelastic, a proper constitutive equation describing the rheology of polymer melts must be chosen. The single eXtended Pom-Pom (SXPP) model,[35] which can describe the shear and tensile behavior of thick polymer systems, is used to describe the constitutive relationship of the viscoelastic HDPE melt in this paper, which is givens as follows.

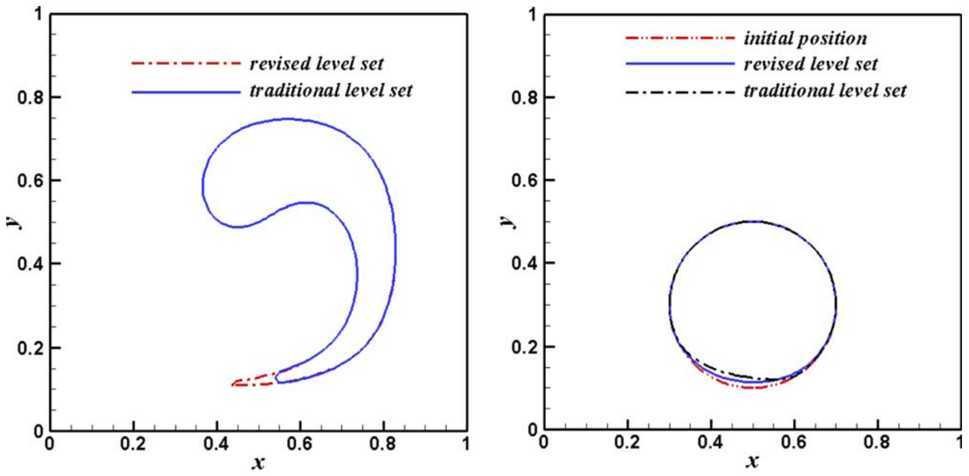

(a). comparison of the results at t=1s (b). t=0s and 2s

Figure 4. Comparison of the results on grid 100 × 100 between the traditional level set method and the revised level set with high resolution scheme. [Color figure can be viewed in the online issue, which is available at wileyonlinelibrary.com.]

$$f(\lambda,\boldsymbol{\tau})\boldsymbol{\tau}+\lambda_{0b}\,\boldsymbol{\tau}\nabla+G_0(f(\lambda,\boldsymbol{\tau})-1)\mathbf{I}+\frac{\alpha}{G_0}\boldsymbol{\tau}\cdot\boldsymbol{\tau}=2\lambda_{0b}G_0\mathbf{D} \tag{11}$$

where

$$f(\lambda,\boldsymbol{\tau})=2\frac{\lambda_{0b}}{\lambda_{0s}}e^{v(\lambda-1)}\left(1-\frac{1}{\lambda}\right)+\frac{1}{\lambda^2}\left[1-\frac{\alpha\mathbf{I}_{\tau\cdot\tau}}{3G_0^2}\right],\ \lambda=\sqrt{1+\frac{|\boldsymbol{I}_\tau|}{3G_0}},\ v=\frac{2}{q}.$$

Here, λ is the backbone stretch used to represent the stretching degree of the polymer molecule; $\boldsymbol{\tau}$ is the stress tensor; λ_{0b} and λ_{0s} denote the orientation and backbone stretch relaxation time-scales of the polymer chains, respectively; G_0 is the linear relaxation modulus; $\mathbf{I}$ is the identity tensor; α is a material parameter defining the amount of anisotropy; $\mathbf{D}$ is the strain tensor; q is the number of arms of the polymer chains; and the superscript symbol ∇ over $\boldsymbol{\tau}$ represents the upper-convected derivative, defined as

$$\boldsymbol{\tau}\nabla=\frac{\partial}{\partial t}\boldsymbol{\tau}+\mathbf{u}\cdot\nabla\boldsymbol{\tau}-(\nabla\mathbf{u})^T\cdot\boldsymbol{\tau}-\boldsymbol{\tau}\cdot(\nabla\mathbf{u})$$

Equations (7–11) can be written in dimensionless form by introducing the dimensionless variables

$$x=Lx',\ y=Ly',\ u=Uu',\ v=Uv',\ t=(L/U)\,t',\ p=p'\rho_mU^2,$$
$$\rho=\rho_m\rho',\ \eta=\eta_m\eta',\tau_{ik}=\eta_mU\tau'_{ik}/L,\ C=C_mC',\ K=K_mK',\ T=T_0T'$$

Where the primes denote dimensionless variables. Substituting these dimensionless variables into eqs. (7)–(11) and dropping the primes, we have

Continuity equation

$$\frac{\partial\rho}{\partial t}+\frac{\partial(\rho u)}{\partial x}+\frac{\partial(\rho v)}{\partial y}=0 \tag{12}$$

u-momentum equation

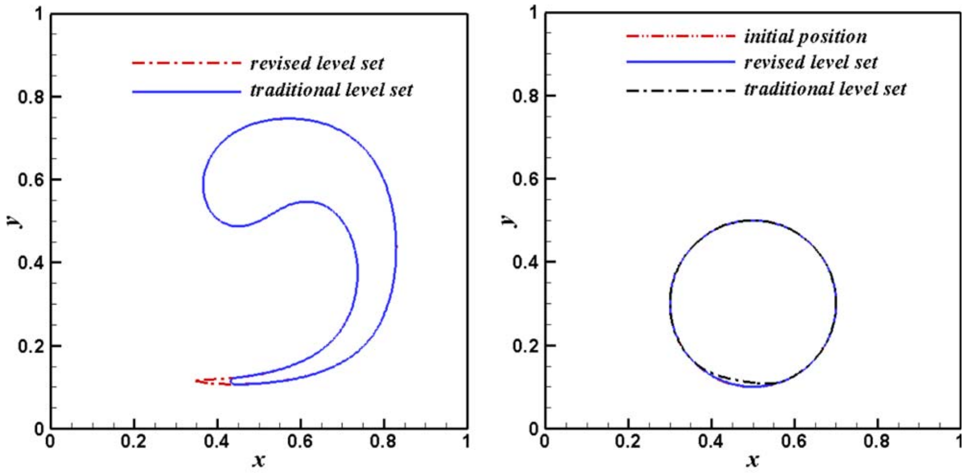

(a). comparison of the results at t=1s (b). t=0s and 2s

Figure 5. Comparison of the results on grid 200 × 200 between the traditional level set method and the revised level set with high resolution scheme. [Color figure can be viewed in the online issue, which is available at wileyonlinelibrary.com.]

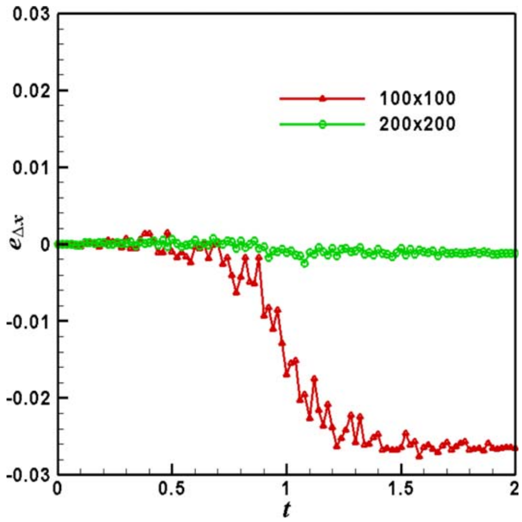

Figure 6. The errors $e_{\Delta x}$ changes versus time under two different grids using the revised level set method with high resolution scheme. [Color figure can be viewed in the online issue, which is available at wileyonlinelibrary.com.]

$$\frac{\partial(\rho u)}{\partial t}+\frac{\partial(\rho uu)}{\partial x}+\frac{\partial(\rho vu)}{\partial y}-\frac{1}{Re}\left(\frac{\partial^2(\eta u)}{\partial x^2}+\frac{\partial^2(\eta u)}{\partial y^2}\right)= -\frac{\partial p}{\partial x}+\frac{(\beta-1)}{Re}\left(\frac{\partial^2(\eta u)}{\partial x^2}+\frac{\partial^2(\eta u)}{\partial y^2}\right)H_\varepsilon(\phi) +\frac{1}{Re}\frac{\partial\tau_{xx}}{\partial x}H_\varepsilon(\phi)+\frac{1}{Re}\frac{\partial\tau_{xy}}{\partial y}H_\varepsilon(\phi) \tag{13}$$

v-momentum equation

$$\frac{\partial(\rho v)}{\partial t}+\frac{\partial(\rho uv)}{\partial x}+\frac{\partial(\rho vv)}{\partial y}-\frac{1}{Re}\left(\frac{\partial^2(\eta v)}{\partial x^2}+\frac{\partial^2(\eta v)}{\partial y^2}\right)= -\frac{\partial p}{\partial y}+\frac{(\beta-1)}{Re}\left(\frac{\partial^2(\eta v)}{\partial x^2}+\frac{\partial^2(\eta v)}{\partial y^2}\right)H_\varepsilon(\phi) +\frac{1}{Re}\frac{\partial\tau_{yx}}{\partial x}H_\varepsilon(\phi)+\frac{1}{Re}\frac{\partial\tau_{yy}}{\partial y}H_\varepsilon(\phi) \tag{14}$$

Constitutive equation

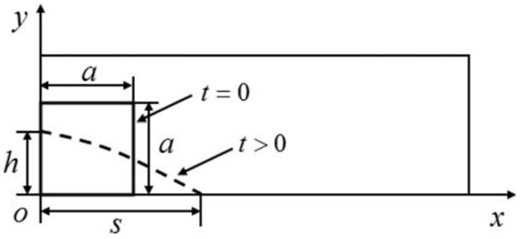

Figure 7. Schematic for two-dimensional broken dam problem.

$$m\frac{\partial\psi}{\partial t}+\nabla\cdot(m\mathbf{u}\psi)-\nabla\cdot(\Lambda\nabla\psi)=S_\psi \tag{15}$$

Energy equations

$$Pe\left(\frac{\partial}{\partial t}(\rho CT)+\nabla\cdot(\rho C\mathbf{u}T)\right)=\nabla\cdot(K\nabla T)+Br(\boldsymbol{\sigma}:\mathbf{D}) \tag{16}$$

The constants and functions in eq. (15) are defined in Table I.[36] Here, the Reynolds number $Re=\rho_m LU/\eta_m$, the Peclet number $Pe=\rho_m C_m UL/K_m$, the Brinkman number $Br=\eta_m U^2/K_m T_0$ and the Weissenberg number $Wi=\lambda_{0b}U/L$. Furthermore,

$$\begin{aligned}\rho(\phi)&=\rho_g/\rho_m+\left(1-\rho_g/\rho_m\right)H_\varepsilon(\phi)\\ \eta(\phi)&=\eta_g/\eta_m+\left(1-\eta_g/\eta_m\right)H_\varepsilon(\phi)\\ C(\phi)&=C_g/C_m+\left(1-C_g/C_m\right)H_\varepsilon(\phi)\\ K(\phi)&=K_g/K_m+\left(1-K_g/K_m\right)H_\varepsilon(\phi)\end{aligned}$$

Phase Change Model

Various models and methods have been proposed to describe phase changes, such as the Stefan model,[37–39] the enthalpy model[12,40–44] and the phase-field model.[45] The enthalpy model must include the relationship between enthalpy H and temperature T for both the melt phase and the air phase. In our previous work,[37] a revised enthalpy method was established to describe the latent heat for the viscoelastic melt and the air simultaneously in the cavity. In this article, we use the revised enthalpy model to describe the latent heat for the viscoelastic melt and the air in the cavity.

Defining $C(T)=\frac{\partial H}{\partial T}$, the transformation relationship between enthalpy H and temperature T is given as follows.

$$T(H)=\begin{cases}T_s+\dfrac{H}{C_s} & H\le 0\\[2ex] T_s+\dfrac{H(T_l-T_s)}{L_H+C_h(T_l-T_s)} & 0<H<L_H+C_h(T_l-T_s)\\[2ex] T_s+\dfrac{H}{C_s}-\dfrac{L_H+(C_h-C_l)(T_l-T_s)}{C_l} & H\ge L_H+C_h(T_l-T_s)\end{cases} \tag{17}$$

We have

$$T_s=T_g+(T_{m,s}-T_g)H_\varepsilon(\phi)\quad T_l=T_g+(T_{m,l}-T_g)H_\varepsilon(\phi)$$
$$L_H=L_g+(L_m-L_g)H_\varepsilon(\phi)$$

$$C_s=C_g+(C_{m,s}-C_g)H_\varepsilon(\phi)\quad C_h=C_g+(C_{m,h}-C_g)H_\varepsilon(\phi)$$
$$C_l=C_g+(C_{m,l}-C_g)H_\varepsilon(\phi)$$

where the subscripts m, g represent the melt phase and the gas phase in the cavity, respectively. The subscripts s, h, l represent the solid, mush and liquid states of the polymer melt, respectively. T_g is the gas-phase temperature. $T_{m,s}$, $T_{m,l}$ is the temperature threshold of the solid and liquid states for the melt phase,

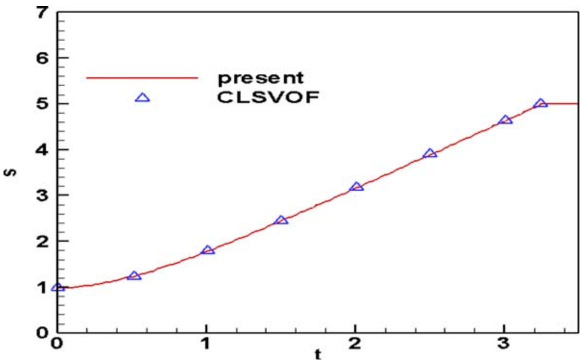

Figure 8. Surge front position *s* along *h* versus time. [Color figure can be viewed in the online issue, which is available at wileyonlinelibrary.com.]

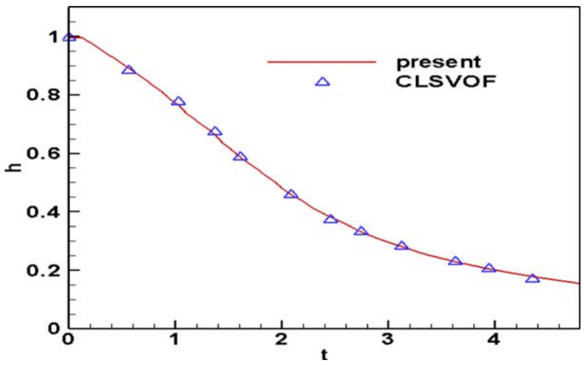

Figure 9. Remaining water column height *x*-direction versus time.[Color figure can be viewed in the online issue, which is available at wileyonline-library.com.]

respectively. L_H is the latent heat. L_m, L_g are the latent heat values of the melt phase and gas phase, respectively. C_g is the change rate of the gas enthalpy change with temperature. $C_{m,s}$ is the change rate of the enthalpy change with temperature when the melt is in the solid state. The meanings of $C_{m,h}$ and $C_{m,l}$ are analogous to that of $C_{m,s}$ Thus, these expressions describe the relationship between H and T for the melt when $H_\varepsilon(\phi)=1$ and for the air in the cavity when $H_\varepsilon(\phi)=0$.

Introducing the Kirchhoff temperature $T_{kir}=\Gamma(H)H+S(H)$, the expression of the enthalpy model can be given as follows.

$$Pe\left(\frac{\partial\rho H}{\partial t}+\frac{\partial\rho uH}{\partial x}+\frac{\partial\rho vH}{\partial y}\right)=\frac{\partial^2\Gamma(H)H}{\partial x^2}+\frac{\partial^2\Gamma(H)H}{\partial y^2}+\frac{\partial^2 S(H)}{\partial x^2}+\frac{\partial^2 S(H)}{\partial y^2}+Br(\boldsymbol{\sigma}:\mathbf{D}) \tag{18}$$

in which

$$\Gamma(H)=\begin{cases}\dfrac{K_s}{C_s} & H\le 0\\[2ex] \dfrac{k_h(T_l-T_s)}{L_H+C_h(T_l-T_s)} & 0<H<L_H+C_h(T_l-T_s)\\[2ex] \dfrac{K_l}{C_l} & H\ge L_H+C_h(T_l-T_s)\end{cases}$$

$$S(H)=\begin{cases}0 & H\le 0\\ 0 & 0<H<L_H+C_h(T_l-T_s)\\ -K_l\dfrac{L_H+(C_h-C_l)(T_l-T_s)}{C_l} & H\ge L_H+C_h(T_l-T_s)\end{cases}$$

and

$$K_s=K_g+(K_{m,s}-K_g)H_\varepsilon(\phi)\ K_h=K_g+(K_{m,h}-K_g)H_\varepsilon(\phi)$$
$$K_l=K_g+(K_{m,l}-K_g)H_\varepsilon(\phi)$$

where K_g is the thermal conductivity of gas. $K_{m,s}$, $K_{m,h}$, and $K_{m,l}$ are the thermal conductivity when the melt phases are solid, mush and liquid, respectively.

Cross-WLF Model

The Cross-WLF model, which is the most appropriate model for studying both the filling and the packing phases, has been chosen to assess the total viscosity η of the polymer melt and better adjust the temperature and pressure sensitivities of the zero-shear-rate viscosity.[46] It specifies that

$$\eta_l(T,\dot\gamma,p)=\frac{\eta_0(T,p)}{1+(\eta_0\dot\gamma/\tau^*)^{1-n_0}} \tag{19}$$

where $\dot\gamma$ is the shear rate. τ^* is a constant that gives the shear stress rate at which the pseudoplastic behaviour of the melt begins. n_0 is the non-Newtonian index. $\eta_0(T,p)$ is the melt viscosity under the zero-shear-rate condition and is a function of temperature and pressure; it reflects the influence of temperature and pressure on the melt viscosity.

The WLF expression determines the viscosity of the melt under zero-shear-rate conditions

$$\eta_0=D_1\exp\left[\frac{-A_1(T-T^*)}{A_2+(T-T^*)}\right] \tag{20}$$

where $T^*=D_2+D_3p$, $A_2=\hat{A}_2+D_3p$. The constant A_1 is the temperature dependence of the melt glass transition temperature under zero-shear-rate conditions. The value of parameter $\hat{A}_2$ depends on the type of polymer melt considered. The constant D_1 is the melt viscosity under zero-shear-rate conditions at the melt glass transition temperature and atmospheric pressure. D_2 is the glass transition temperature. D_3 is the variation of the glass transition temperature of the melt with pressure. T^* is the glass transition temperature of the melt, depending on the pressure.

Boundary Conditions and Time Step

Proper boundary conditions must be posed on the solid walls of the cavity. We used the boundary conditions proposed by Yang *et al.* for two-phase flow.[20]

1. On the wall of the cavity, for the melt in the cavity, no-slip boundary conditions are used for the velocities, that is, $u=v=0$; for the gas in the cavity, $\frac{\partial u}{\partial \mathbf{n}}=\frac{\partial v}{\partial \mathbf{n}}=0$.
2. On the wall of the cavity, for the melt in the cavity, no-penetration boundary conditions are used for the pressure, that is, $\frac{\partial p}{\partial \mathbf{n}}=0$; for the gas in the cavity, we use $P=0$.

The time step Δt is determined by the restrictions resulting from the Courant-Friedrichs-Lewy (CFL) condition and viscosity.[33] Define

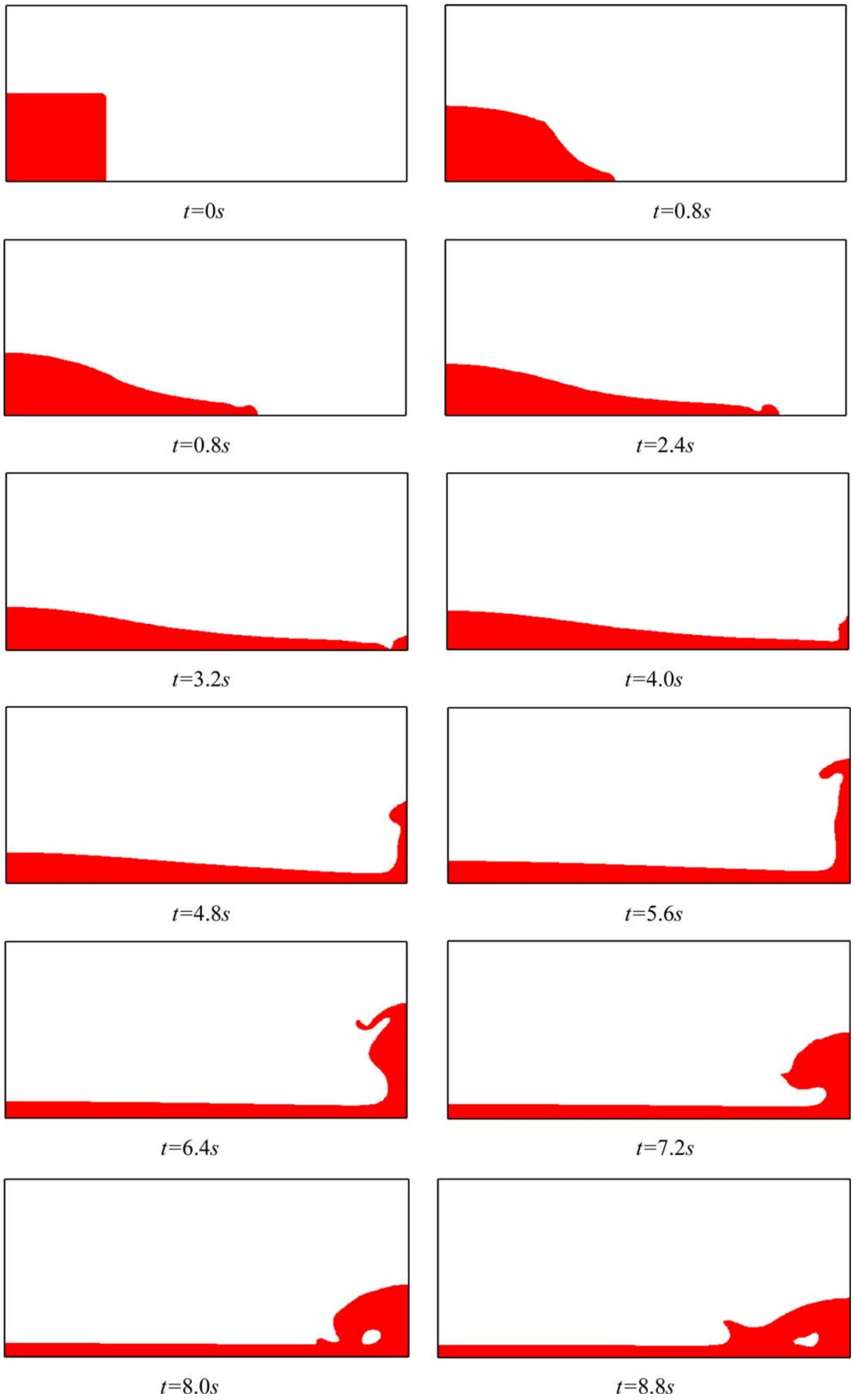

t=0*s* *t*=0.8*s*

t=0.8*s* *t*=2.4*s*

t=3.2*s* *t*=4.0*s*

t=4.8*s* *t*=5.6*s*

t=6.4*s* *t*=7.2*s*

t=8.0*s* *t*=8.8*s*

Figure 10. The position of the free surface water bodies in different time (shaded areas denote the water). [Color figure can be viewed in the online issue, which is available at wileyonlinelibrary.com.]

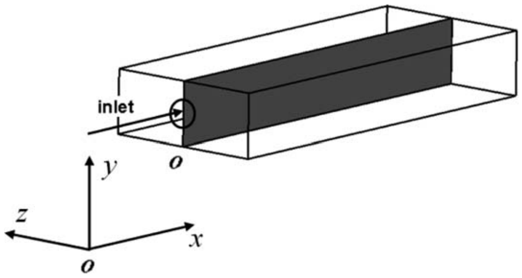

Figure 11. Sketch map and computational area (shaded area) of the mold.

$$\Delta t_c=\min\left(\frac{\Delta x}{|\mathbf{u}|}\right)\quad \Delta t_\eta=\min\left(\frac{3}{14}\frac{\rho Re\Delta x^2}{\eta}\right)$$

The overall restriction on the time step is then

$$\Delta t=\frac{1}{2}\min\left(\Delta t_c,\Delta t_\eta\right)$$

FIBER DYNAMICS

We used the method proposed by Yang *et al.*[47] to simulate the dynamics of fibers, which include the translation and orientation processes caused by the force imposed on the fibers by the melt.

Translation Motion of the Fibers

The translation motion of fiber i is described by Newton's law of motion, which is expressed as follows.

$$\mathbf{F}_i=m_i\frac{d\mathbf{u}_i}{dt} \tag{21}$$

where $\mathbf{F}_i$ is the resultant force imposed on fiber i and $\mathbf{F}_i=((F_x)_i,(F_y)_i)$, m_i is the mass of fiber i and $\mathbf{u}_i=(u_i,v_i)$ is the velocity of fiber i. The velocity $\mathbf{u}_i$ at the $(n+1)$th step can be obtained using eq. (22).

$$\mathbf{u}_i^{n+1}=\mathbf{u}_i^n+\frac{\mathbf{F}_i\Delta t}{m_i} \tag{22}$$

where $\mathbf{u}_i^n$ is the velocity of fiber i at the nth step and Δt is the time step.

Several different forces may be imposed on each fiber. This paper considers the drag and pressure gradient forces, which are the major forces imposed on the fibers.

The drag force can be expressed as[48]

$$(\mathbf{F}_d)_i=(C_d)_i(A_p)_i\rho_l|\mathbf{u}_l-\mathbf{u}_i|(\mathbf{u}_l-\mathbf{u}_i)/2 \tag{23}$$

where $(\mathbf{F}_d)_i$ is the drag force and $(C_d)_i$ is the coefficient of the drag force for fiber i. $(A_p)_i$ is the projected surface area of the fiber normal to the direction of its motion. $\mathbf{u}_l$ is the polymer melt velocity. The choice of C_d is very important for the computation of the drag force. The formula for C_d used in this article is[48]

$$C_d=\frac{24}{Re_f}\frac{d_A}{d_n}\left(1+\frac{0.15}{\sqrt{c}}\left(\frac{d_A}{d_n}Re_f\right)^{0.687}\right)+\frac{0.42\left(\frac{d_A}{d_n}\right)^2}{\sqrt{c}\left(1+4.25\times10^4\left(\frac{d_A}{d_n}Re_f\right)^{-1.16}\right)} \tag{24}$$

where Re_f is the Reynolds number of the fiber. $d_A=\sqrt{4A_p/\pi}$ is the surface equivalent sphere diameter. $d_n=\sqrt[3]{6V_f/\pi}$ is the volume equivalent sphere diameter or nominal diameter. V_f is the fiber volume, and c is the fiber circularity. The relationship between the fiber circularity c and fiber aspect ratio r_c is $c=2.62{r_c}^{2/3}/(1+2r_c)$. The Reynolds number $(Re_f)_i$ of fiber i can be computed as follows.

$$\left(Re_f\right)_i=\frac{\rho_l|\mathbf{u}_{\text{vir}}-\mathbf{u}_i|(d_n)_i}{\eta_l} \tag{25}$$

where $\mathbf{u}_{\text{vir}}$ is the virtual velocity at the centroid of fiber i and $\mathbf{u}_{\text{vir}}$ can be computed by the bilinear interpolation formula.[49] d_n is the diameter of fiber i. η_l is the viscosity of the fluid.

The expression of the pressure gradient force is $(V_f)_i\nabla p_i$. Enclosing the drag force and the pressure gradient force, the resultant force $\mathbf{F}_i$ imposed on fiber i can be expressed as

$$\mathbf{F}_i=(\mathbf{F}_d)_i+(V_f)_i\nabla p_i \tag{26}$$

The new position of fiber i at the $(n+1)$th step can be expressed as follows.

$$\mathbf{W}_i^{n+1}=\mathbf{W}_i^n+\mathbf{u}_i^{n+1}\Delta t \tag{27}$$

where $\mathbf{W}_i=(W_x,W_y)$ is the position vector of fiber i and $\mathbf{W}_i^n$ is the position of fiber i at the nth step.

Fiber Orientation

The orientation of a fiber can be expressed in three-dimensional space coordinates as shown in Figure 1. Because the fiber has a circular cross-section and does not bend, the orientation is determined by ϕ and ϖ. ϕ is the angle between x-axis and the projection of the fiber on x-y plane. ϖ is the angle between the fiber vector and z-axis.

Jeffery's equation describes the orientation of a fiber as[50]

$$\dot{\mathbf{R}}=\boldsymbol{\omega}\cdot\mathbf{R}+\lambda_f(\boldsymbol{\varepsilon}\cdot\mathbf{R}-\boldsymbol{\varepsilon}:\mathbf{RRR}) \tag{28}$$

where $\mathbf{R}$ is the unit vector aligned with the fiber axis. A dot over a variable denotes the time derivative throughout this paper. $\boldsymbol{\omega}=(\nabla\mathbf{u}^{\mathrm{T}}-\nabla\mathbf{u})/2$, $\boldsymbol{\varepsilon}=(\nabla\mathbf{u}^{\mathrm{T}}+\nabla\mathbf{u})/2$ is the deformation rate tensor, $\lambda_f=(r_c^2-1)/(r_c^2+1)$. Zhou and Lin[51] derived the fiber orientation distribution based on classic mechanics and kinetic theory. They depict the fiber orientation for a planar flow field aligned with the x-y plane. For convenience, we denote

Table II. Material Properties of HDPE[56]

Parameter (unit)	ρ_m (kg m^{-3})	n_0	τ^* (Pa)	D_1 (Pa s)	D_2 (K)	D_3 (Pa K^{-1})	A_1	$\tilde{A}_2$ (K)
Value	1.02	0.3794	105,985	5.769 × 103	233.15	0.1	32.344	51.6

Table III. Thermal Property Parameters of HDPE[56]

Parameter (unit)	$K_{m,s}$ (W m^{-1} °C^{-1})	$K_{m,f}$ (W m^{-1} °C^{-1})	$K_{m,l}$ (W m^{-1} °C^{-1})	$C_{m,s}$ (·kg^{-1} °C^{-1})	$C_{m,f}$ (J kg^{-1} °C^{-1})	$C_{m,l}$ (J kg^{-1} °C^{-1})	L_m (J kg^{-1})	$T_{m,s}$ (°C)	$T_{m,l}$ (°C)
Value	0.316	0.298	0.238	2042	2516	2990	1.8 × 105	104	108

$$\frac{\partial u}{\partial x}=j\dot{\gamma}\;\frac{\partial u}{\partial y}=\dot{\gamma}\;\frac{\partial v}{\partial x}=k\dot{\gamma}\;\frac{\partial v}{\partial y}=-j\dot{\gamma}$$

The variance ratio of $\dot{\varphi}$ and θ can then be expressed as follows according to Jeffery's equation.[51]

$$\dot{\varphi}=\frac{1}{2}\left[\lambda_f(k+1)\cos(2\varphi)+k-1-2\lambda\sin(2\varphi)\right]\dot{\gamma} \tag{29}$$

$$\dot{\theta}=\frac{1}{4}\lambda_f\sin(2\theta)[2j\cos(2\varphi)+(k+1)\sin(2\varphi)]\dot{\gamma} \tag{30}$$

Effect of Fibers on Polymer Flow

The influence of fibers on the fluid flow is described by the momentum exchange source term in the model. The momentum exchange source term $\mathbf{S}_P=((S_P)_x,(S_P)_y)^T$ is added to the momentum eqs. (13) and (14) as follows.

u-momentum equation

$$\frac{\partial(\rho u)}{\partial t}+\frac{\partial(\rho uu)}{\partial x}+\frac{\partial(\rho vu)}{\partial y}-\frac{1}{Re}\left(\frac{\partial^2(\mu u)}{\partial x^2}+\frac{\partial^2(\mu u)}{\partial y^2}\right)=-\frac{\partial p}{\partial x}H_\varepsilon(\phi)$$
$$+\frac{(\beta-1)}{Re}\left(\frac{\partial^2(\mu u)}{\partial x^2}+\frac{\partial^2(\mu u)}{\partial y^2}\right)H_\varepsilon(\phi)+\frac{1}{Re}\frac{\partial\tau_{xx}}{\partial x}H_\varepsilon(\phi)$$
$$+\frac{1}{Re}\frac{\partial\tau_{xy}}{\partial y}H_\varepsilon(\phi)-(S_p)_xH_\varepsilon(\phi) \tag{31}$$

v-momentum equation

$$\frac{\partial(\rho v)}{\partial t}+\frac{\partial(\rho uv)}{\partial x}+\frac{\partial(\rho vv)}{\partial y}-\frac{1}{Re}\left(\frac{\partial^2(\mu v)}{\partial x^2}+\frac{\partial^2(\mu v)}{\partial y^2}\right)=-\frac{\partial p}{\partial y}H_\varepsilon(\phi)$$
$$+\frac{(\beta-1)}{Re}\left(\frac{\partial^2(\mu v)}{\partial x^2}+\frac{\partial^2(\mu v)}{\partial y^2}\right)H_\varepsilon(\phi)+\frac{1}{Re}\frac{\partial\tau_{yx}}{\partial x}H_\varepsilon(\phi)$$
$$+\frac{1}{Re}\frac{\partial\tau_{yy}}{\partial y}H_\varepsilon(\phi)-(S_p)_yH_\varepsilon(\phi) \tag{32}$$

The momentum exchange source term $\mathbf{S}_p$ in a control volume (width Δx and height Δy) is calculated as

$$\mathbf{S}_p=\frac{1}{V_{\text{cell}}}\sum_{i=1}^{N^*}\mathbf{F}_i \tag{33}$$

Here, N^* is the number of fibers in this control volume, $\mathbf{F}_i$ is the resultant force imposed on fiber i in this control volume and $V_{\text{cell}}=\Delta x\Delta y$ is the area of the control volume.

Table IV. Thermal Property Parameters of Air in the Cavity[56]

Parameter (unit)	K_g (W m^{-1} °C^{-1})	C_g (J kg^{-1} °C^{-1})	L_g (J kg^{-1})	T_g (K)
Value	0.023	1000	2260	T_{wall}

Equations (1), (4), (12), (15), (18–20), (31), and (32) and the boundary conditions compose the model for the gas-solid-liquid three-phase model for the simulation of the fiber-reinforced polymer mold-filling process considering phase change. The coupling relationship between the equations is shown in Figure 2.

NUMERICAL METHOD

Discretization

The finite volume SIMPLE methods on a non-staggered grid are used to solve the governing eqs. (12), (15), (18), (31), and (32). A nonstaggered grid arrangement, which stores all the variables at the same physical location and employs only one set of control volumes, is shown in Figure 3, where the dashed lines are the faces of control volumes or cells and the intersection points of the solid lines are the nodes on which all the physical quantities are located.[37,52]

Continuity Equation

The continuity eq. (12) can be discretized to be the following form by integrating in the control volume

$$[(\rho u)_e-(\rho u)_w]\Delta y+[(\rho u)_n-(\rho u)_s]\Delta x=0 \tag{34}$$

Momentum Equations

The discretization of the momentum eqs. (31) and (32) can be written as the following form by a generalized quantity ψ, that is,

$$a_P\psi_P=a_E\psi_E+a_W\psi_W+a_N\psi_N+a_S\psi_S+S_\psi \tag{35}$$

where S_ψ is the source term in the momentum equation. The coefficients a_E, a_W, a_N, a_S, a_P can be expressed as the combination of the convection term and the diffusion term, that is,

$$a_E=D_eA(|P_e|)+\max(-F_e,0),\; a_W=D_wA(|P_w|)+\max(F_w,0),$$
$$a_N=D_nA(|P_n|)+\max(-F_n,0)$$

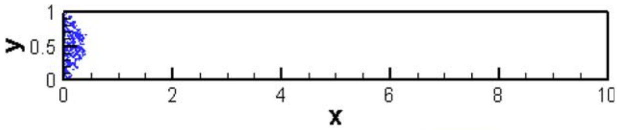

(a) Distribution of initial generated fibers.

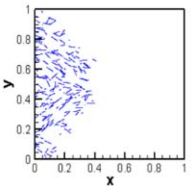

(b) A partial enlargement of Figure 12(a).

Figure 12. Distribution of initial generated fibers. [Color figure can be viewed in the online issue, which is available at wileyonlinelibrary.com.]

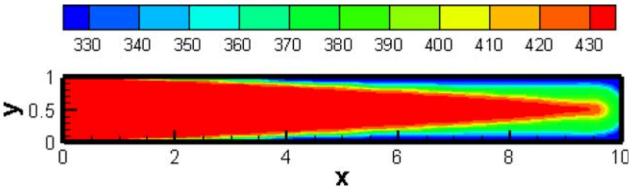

Figure 13. Temperature distribution at the end of the mold-filling process ($T_{\text{wall}} = 303$ K, $T_{\text{melt}} = 433$ K, $u = -4.0 \times (y-0.5)^2 + 1, y \in [0,1], t = 7546\ \Delta t$). [Color figure can be viewed in the online issue, which is available at wileyonlinelibrary.com.]

$$a_S = D_s A(|P_s|) + \max(F_s, 0),\quad a_P = a_E + a_W + a_N + a_S + \Delta x \Delta y \rho / \Delta t$$

where P_e, P_s, P_w, P_n are the Peclet numbers on the cell faces, F_e, F_s, F_w, F_n are the cell faces flux, and D_e, D_s, D_w, D_n denote diffuse derivatives on cell faces. The form of $A(|P_e|)$ can be different under different discretization schemes for the convection term. For example, $A(|P_\Delta|)\mathrm{A}(|\mathrm{P}_\Delta|)$ equals to 1 for the upwind scheme while $1-0.5|P_\Delta|\ 1-0.5|\mathrm{P}_\Delta|$ for a central scheme. We take $A(|P_\Delta|)=1\ \mathrm{A}(|\mathrm{P_e}|)=1$ in this article. All the coefficients are formulated as follows.

$$F_e = (\rho u)_e \Delta y \quad D_e = \frac{\eta_e \Delta y}{(x_E - x_P)Re} \quad P_e = \frac{F_e}{D_e} \tag{36a}$$

$$F_w = (\rho u)_w \Delta y \quad D_w = \frac{\eta_w \Delta y}{(x_P - x_W)Re} \quad P_w = \frac{F_w}{D_w} \tag{36b}$$

$$F_n = (\rho v)_n \Delta x \quad D_n = \frac{\eta_n \Delta x}{(y_N - y_P)Re} \quad P_n = \frac{F_n}{D_n} \tag{36c}$$

$$F_s = (\rho v)_s \Delta x \quad D_s = \frac{\eta_s \Delta x}{(y_P - y_S)Re} \quad P_s = \frac{F_s}{D_s} \tag{36d}$$

Constitutive Equations

The discretization of the constitutive eq. (15) can also be written as the following form by a generalized quantity, that is,

$$a_P^\tau \psi_P = a_E^\tau \psi_E + a_W^\tau \psi_W + a_N^\tau \psi_N + a_S^\tau \psi_S + S_\psi^\tau \tag{37}$$

where S_ψ^τ is the source term in the constitutive equation and the coefficients $a_E^\tau, a_W^\tau, a_N^\tau, a_S^\tau, a_P^\tau$ can be expressed as

$$a_E^\tau = Wi\max(-F_e, 0),\ a_W^\tau = Wi\max(F_w, 0),\ a_N^\tau = Wi\max(-F_n, 0),$$

$$a_S^\tau = Wi\max(F_s, 0),\ a_P^\tau = a_E^\tau + a_W^\tau + a_N^\tau + a_S^\tau + Wi\frac{\Delta x \Delta y}{\Delta t}$$

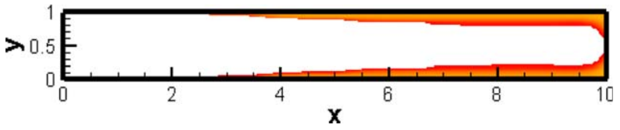

Figure 14. Frozen skin layer at the end of the mold-filling process ($T_{\text{wall}} = 303$ K, $T_{\text{melt}} = 433$ K, $u = -4.0 \times (y-0.5)^2 + 1, y \in [0,1], t = 7546\ \Delta t$). [Color figure can be viewed in the online issue, which is available at wileyonlinelibrary.com.]

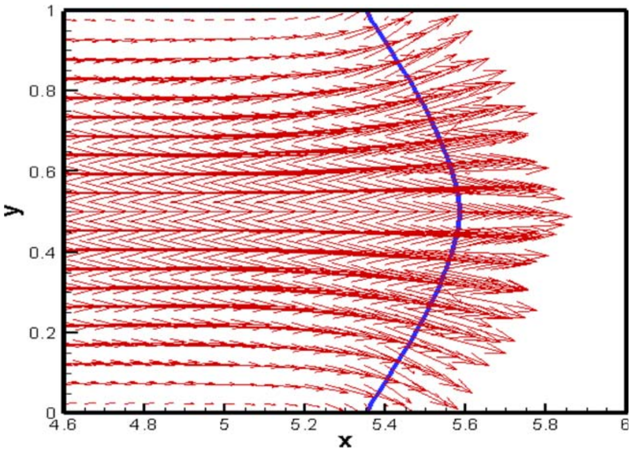

Figure 15. Fountain flow effect at $t = 4000\ \Delta t$. [Color figure can be viewed in the online issue, which is available at wileyonlinelibrary.com.]

Here, the expressions of *Fe*, *Fs*, *Fw*, and *Fn* are identical to (36). The discrete constitutive eq. (37) can be solved only in the liquid part. However, the free surface stress conditions have to be dealt with as has been done by Sussman *et al.*[31] and Aboubacar *et al.*[36] In this paper, we try to avoid doing this by defining another Weissenberg number $Wi' = Wi \times H_\varepsilon(\phi)$ and let $S'_\psi = S_\psi^\tau \times H_\varepsilon(\phi)$. Equation (37) then change into

$$a_P^\tau \psi_P = a_E^\tau \psi_E + a_W^\tau \psi_W + a_N^\tau \psi_N + a_S^\tau \psi_S + S'_\psi \tag{38}$$

The coefficients $a_E^\tau, a_W^\tau, \cdot a_N^\tau, a_S^\tau, a_P^\tau$ can be expressed as

$$a_E^\tau = Wi' \max(-F_e, 0),\ a_W^\tau = Wi' \max(F_w, 0),$$

$$a_N^\tau = Wi' \max(-F_n, 0),\ a_S^\tau = Wi' \max(F_s, 0)$$

$$a_P^\tau = a_E^\tau + a_W^\tau + a_N^\tau + a_S^\tau + Wi' \frac{\Delta x \Delta y}{\Delta t} + \varepsilon_1$$

where ε_1 is a small positive number for avoiding dividing by zero. Thus the constitutive equation can be regarded to be hold in the whole computational domain. In particular, as for the gas phase in the cavity, eq. (37) will be $\varepsilon_1 \psi_P = 0$, which implies $\psi_P = 0$. By doing this, we see that the stresses τ_{xx}, τ_{xy} and τ_{yy} will appear only in the melt phase, although the constitutive equations are solved in the whole computational domain. It is worth pointing out that special interpolation technique, proposed by P.J. Oliveira *et al.*[53] is used to compute the stresses at cell faces from stress values at cell centers, which solves the stress-velocity coupling problem successfully.

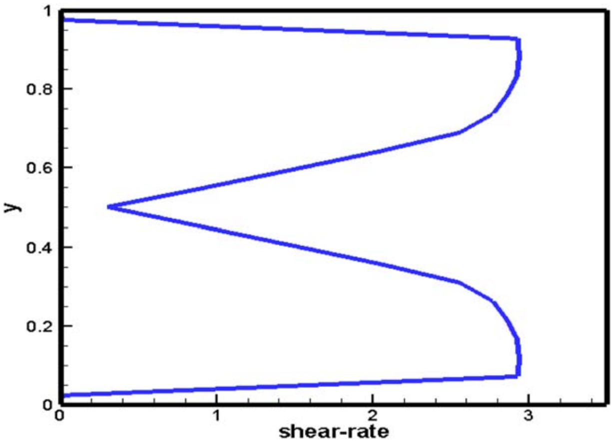

Figure 16. Shear rate distribution at $x = 5$. [Color figure can be viewed in the online issue, which is available at wileyonlinelibrary.com.]

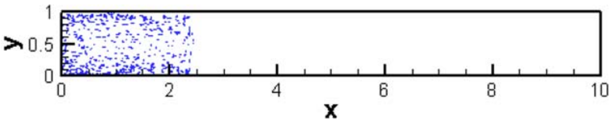

(a) $t=1500\,\Delta t$

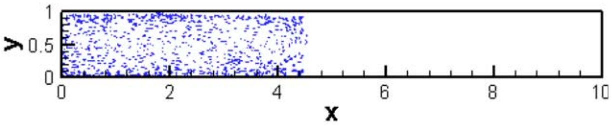

(b) $t=3000\,\Delta t$

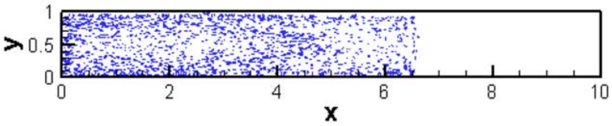

(c) $t=4500\,\Delta t$

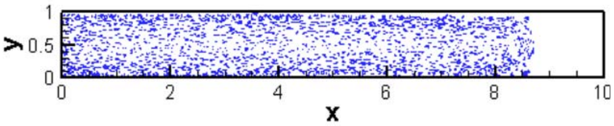

(d) $t=6000\,\Delta t$

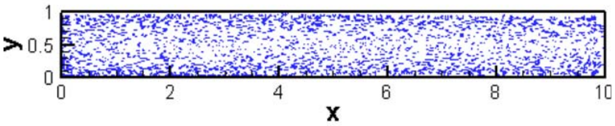

(e) $t=7546\,\Delta t$

Figure 17. Translation and orientation of fibers versus time during mold-filling process. [Color figure can be viewed in the online issue, which is available at wileyonlinelibrary.com.]

Energy Equations

The discretization of the Energy equation can be written as the following form, that is,

$$a_P T_P = a_E T_E + a_W T_W + a_N T_N + a_S T_S + S_T \tag{39}$$

Similarly, the coefficients $a_{E,}\, a_{W,}\, a_{N,}\, a_{S,}\, a_P$ can be expressed as the combination of the convection term and the diffusion term, i.e.

$$a_E D_e A(|P_e|) + \max(-F_e, 0),\ aw = D_w A(|P_w|) + \max(F_w, 0),$$

$$a_N = D_n A(|P_n|) + \max(-F_w, 0)$$

$$a_S D_S A(|P_S|) + \max(-F_e, 0),\ \cdot a_p = a_E + a_W a_N a_S + Pe\Delta x\Delta y\rho/\Delta t$$

where

$$F_e = Pe(\rho u)_e \Delta y \quad D_e = \Gamma(H)\frac{\Delta y}{(x_E - x_P)} \quad P_e = \frac{F_e}{D_e} \tag{40a}$$

$$F_w = Pe(\rho u)_w \Delta y \quad D_w = \Gamma(H)\frac{\Delta y}{(x_P - x_W)} \quad P_w = \frac{F_w}{Dw} \tag{40b}$$

$$F_n = Pe(\rho v)_n \Delta x \quad D_n = \Gamma(H)\frac{\Delta x}{(y_N - y_P)} \quad P_n = \frac{F_n}{D_n} \tag{40c}$$

$$F_s = Pe(\rho v)_s \Delta x \quad D_s = \Gamma(H)\frac{\Delta x}{(y_P - y_S)} \quad P_s = \frac{F_s}{D_s} \tag{40d}$$

Numerical Methods for Level Set and the Reinitialization Equation

Level set evolution eq. (1) and the reinitialization eq. (4) are solved by the finite difference method on a rectangular grid. The spatial derivatives are discretized by the fifth-order weighted essentially nonoscillatory (WENO) scheme and the temporal derivatives are discretized by the 3rd-order Total Variation Diminishing Runge-Kutta (TVD-R-K) scheme.[52,54,55]

WENO Scheme

Define $\phi_{i,j}=\phi(x_i, y_j)$, $\Delta_x^+\phi_{i,j}=\phi_{i+1,j}-\phi_{i,j}$, $\Delta_y^+\phi_{i,j}=\phi_{i,j+1}-\phi$ $i, j\phi_{\mathrm{i,j}}=\phi(x_{\mathrm{i}}, y_{\mathrm{j}})$, $\Delta_x^+\phi_{\mathrm{i,j}}=\phi_{\mathrm{i+1,j}}-\phi_{\mathrm{i,j}}$ then the 5-order WENO scheme for the numerical approximations of the partial derivatives ϕ_x ϕ_x, ϕ_y ϕ_y can be expressed as

$$\phi^{\pm}_{x,i,j} = \frac{1}{12}\left(-\frac{\Delta_x^+\phi_{i-2,j}}{\Delta x} + 7\frac{\Delta_x^+\phi_{i-1,j}}{\Delta x} + 7\frac{\Delta_x^+\phi_{i,j}}{\Delta x} - \frac{\Delta_x^+\phi_{i+1,j}}{\Delta x}\right)$$
$$\pm\Psi^{\mathrm{WENO}}\left(\frac{\Delta_x^-\Delta_x^+\phi_{i\pm2,j}}{\Delta x}, \frac{\Delta_x^-\Delta_x^+\phi_{i\pm1,j}}{\Delta x}, \frac{\Delta_x^-\Delta_x^+\phi_{i,j}}{\Delta x}, \frac{\Delta_x^-\Delta_x^+\phi_{i\mp1,j}}{\Delta x}\right) \tag{41}$$

$$\phi^{\pm}_{y,i,j} = \frac{1}{12}\left(-\frac{\Delta_y^+\phi_{i,j-2}}{\Delta y} + 7\frac{\Delta_y^+\phi_{i,j-1}}{\Delta y} + 7\frac{\Delta_y^+\phi_{i,j}}{\Delta y} - \frac{\Delta_y^+\phi_{i,j+1}}{\Delta y}\right)$$
$$\pm\Psi^{\mathrm{WENO}}\left(\frac{\Delta_y^-\Delta_y^+\phi_{i,j\pm2}}{\Delta y}, \frac{\Delta_y^-\Delta_y^+\phi_{i,j\pm1}}{\Delta y}, \frac{\Delta_y^-\Delta_y^+\phi_{i,j}}{\Delta y}, \frac{\Delta_y^-\Delta_y^+\phi_{i,j\mp1}}{\Delta y}\right) \tag{42}$$

Where, the function Ψ^{WENO} is expressed as

$$\psi^{\mathrm{WENO}}(a, b, c, d) = -\frac{1}{3}w_0(a-2b+c) + \frac{1}{6}\left(w_2 - \frac{1}{2}\right)(b-2c+d)$$

The expressions of w_0, w_2 are

$$\omega_0 = \frac{\alpha_0}{\alpha_0+\alpha_1+\alpha_2},\quad \omega_2 = \frac{\alpha_2}{\alpha_0+\alpha_1+\alpha_2}$$

where

$$\alpha_0 = \frac{1}{(\varepsilon'+S_0)^2},\quad \alpha_1 = \frac{6}{(\varepsilon'+S_1)^2},\quad \alpha_2 = \frac{3}{(\varepsilon'+S_2)^2},$$

$$S_0 = 13(a-b)^2 + 3(a-3b)^2$$

$$S_1 = 13(b-c)^2 + 3(b+c)^2,\quad S_2 = 13(c-d)^2 + 3(3c-d)^2$$

and ε' is a very small number used for avoiding divided by zero.

TVD-R-K Scheme

The 3-order TVD-R-K scheme can be expressed as

$$\phi^{(1)} = \phi^{(0)} + \Delta t L(\phi^{(0)}) \tag{43a}$$

$$\phi^{(2)} = \phi^{(1)} + \frac{\Delta t}{4}\left(-3L\left(\phi^{(0)}\right) + L\left(\phi^{(1)}\right)\right) \tag{43b}$$

$$\phi^{(3)} = \phi^{(2)} + \frac{\Delta t}{12}\left(-L\left(\phi^{(0)}\right) - L\left(\phi^{(1)}\right) + 8L\left(\phi^{(2)}\right)\right) \tag{43c}$$

where $\phi^{(0)}=\phi^{\mathrm{n}}$, $\phi^{(3)}=\phi^{\mathrm{n+1}}$, and $\mathrm{L}(\phi)=-\mathbf{u}\phi_x-\mathrm{v}\phi_y$ for the level set function, while $\mathrm{L}(\phi)=\mathrm{sign}(\phi_0)(1-|\nabla\phi|)$ for the reinitialization equation.

Numerical Tests

Numerical Test for the Rotation Plate Problem. To test the numerical scheme for the level set method, we use the following velocity field on the unit square:

$$u = \pi\cos(\pi(x-0.5))\sin(\pi(y-0.5))$$

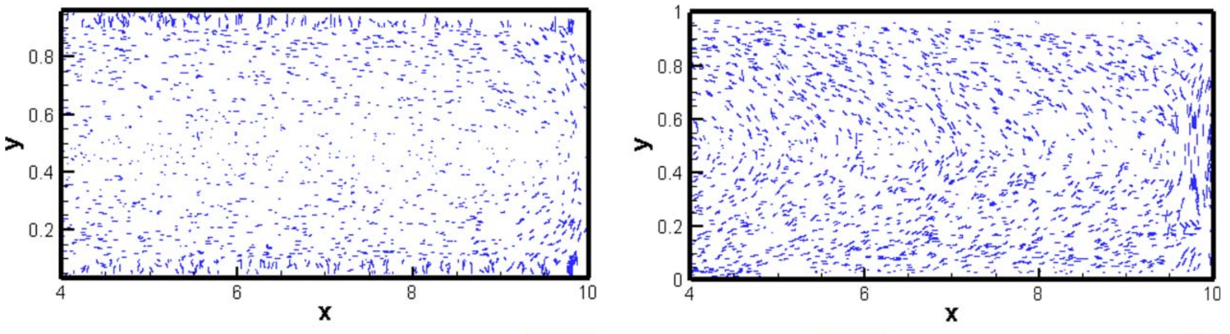

(a) A partial enlargement of Figure 17(e).

(b) Fiber structure of Yang et al.[30]

Figure 18. Comparison of the fiber structure obtained using our model and that of Yang *et al.*[30] [Color figure can be viewed in the online issue, which is available at wileyonlinelibrary.com.]

$$v=-\pi\sin(\pi(x-0.5))\cos(\pi(y-0.5))$$

A circle with radius 0.2 centered at (0.5, 0.3) is used as initial condition. At $t=1.0$, the flow field is reversed, so that the exact solution at $t=2.0$ should coincide with the initial condition. The grids we use are 100 × 100 and 200 × 200, respectively. The comparison between the results of the traditional level set method and the revised method with high resolution method used in this paper with different grids are shown in Figures 4 and 5, and the errors under different grids are given in Figure 6, all of which show the effectiveness of our numerical scheme.

Numerical Test for the Broken Dam Problem

We take the broken dam problem shown in Figure 7[30] to test the validity of the methodology. The computational domain is 4a × 2a, where *a* is the width of the water body. *s* and *h* denote the surge front position and the remaining height of the water column respectively and are used to measure the spreading velocity and the falling rate of the water column. A uniform grid of 500 × 250 is used and we take $a=5$ in the simulation. Figure 8 shows changes of the surge fronts along *x*-direction. Figure 9 shows remaining water column height versus time together with those obtained by a CLSVOF (Coupled level set and Volume of Fluid) method proposed by Sussman *et al.*[31] All the results are in well agreement. Figure 10 gives the positions of the interface at some select times.

RESULTS AND ANALYSIS

Computational Domain and Parameter Setting

A sketch of the injection mold is shown in Figure 11, in which the shaded area, that is, the vertical middle plane of the mold, is the computational domain. Suppose the length and width of computational area are 10.0 and 1.0, respectively. The grid in the simulation is 400 × 40.

High-density polyethylene (HDPE) is used as the polymer melt, and its material properties parameters and thermal property parameters

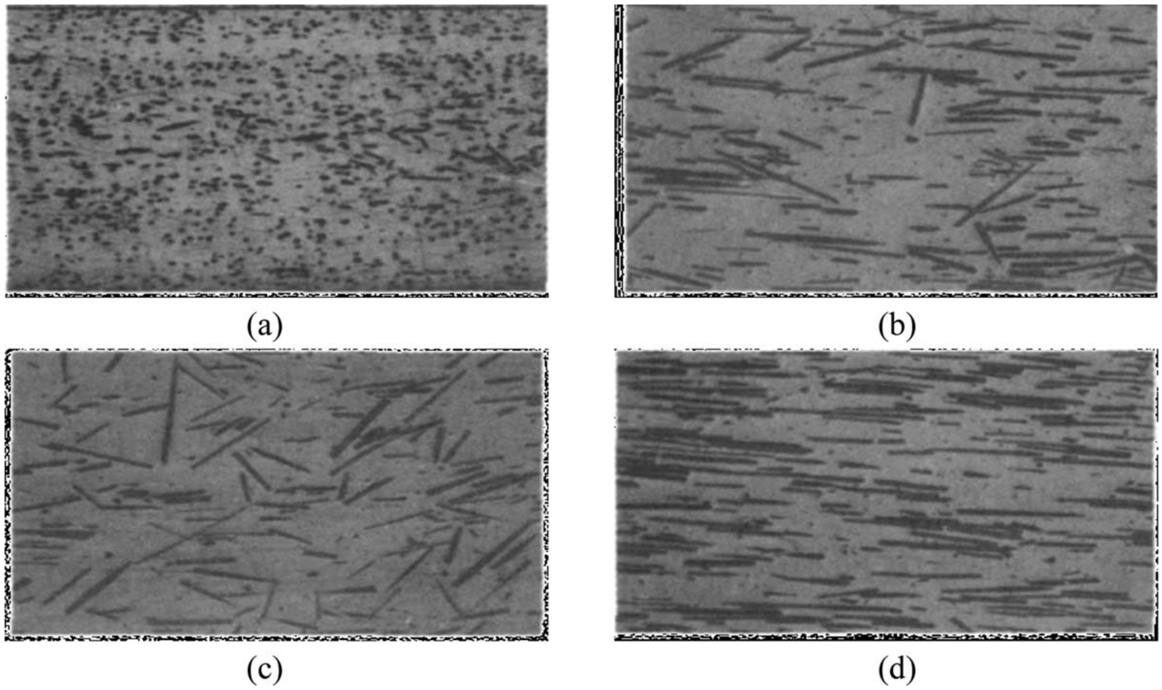

Figure 19. The experimental result of Liu *et al.*[57] (a) Fiber orientation in the cavity(from the view that is perpendicular to the flow direction), (b) Fiber orientation near the surface of the cavity, (c) Fiber orientation near the subsurface of the cavity, and (d) Fiber orientation in the middle of the cavity.

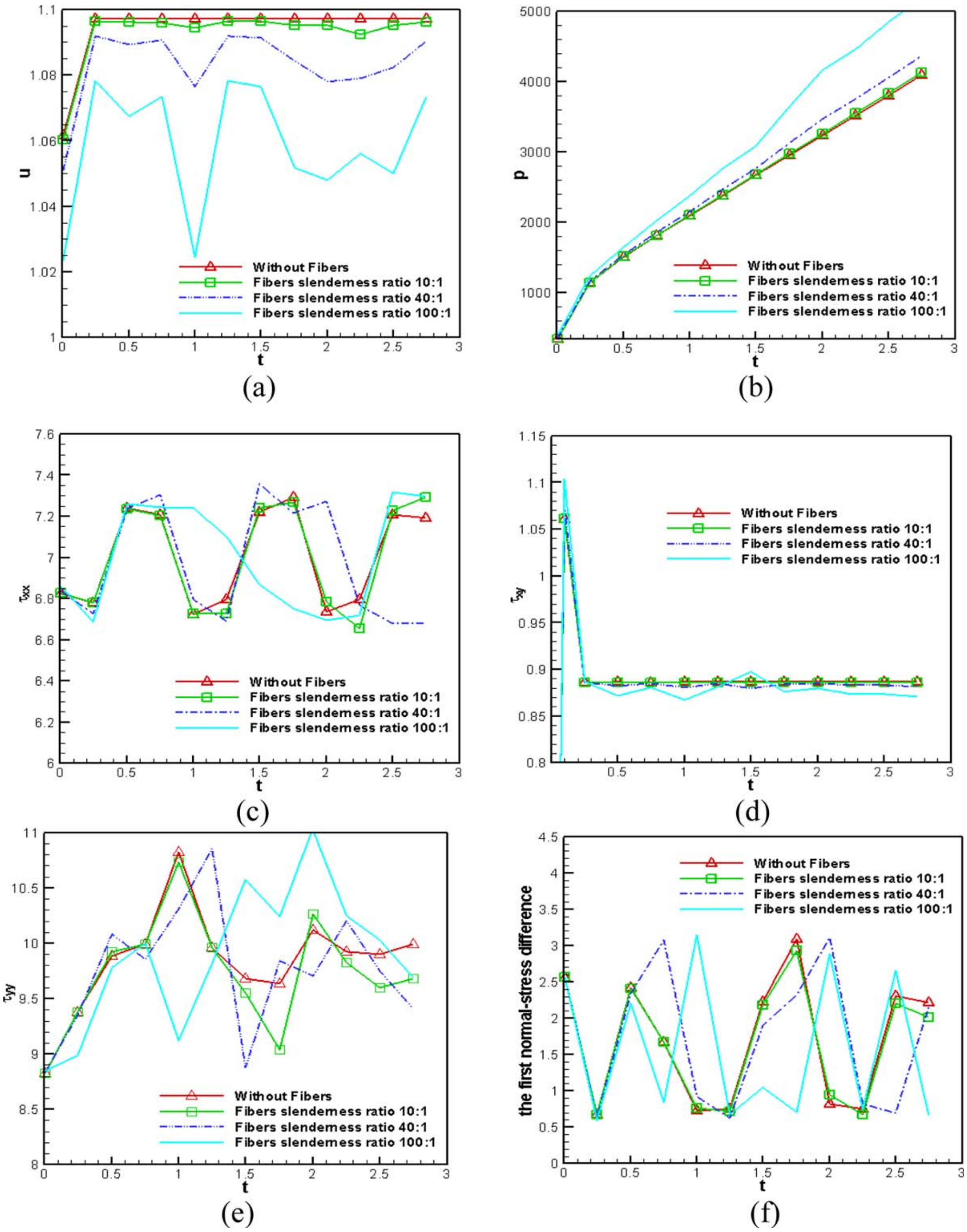

Figure 20. The influence of fiber slenderness ratio on physical quantities versus time. (a) The variation of maximum value of u versus time, (b) The variation of maximum value of p versus time, (c) The variation of maximum value of τ_{xx} versus time, (d) The variation of maximum value of τ_{xy} versus time, (e) The variation of maximum value of τ_{yy} versus time, and (f) The variation of maximum value of first normal-stress difference versus time. [Color figure can be viewed in the online issue, which is available at wileyonlinelibrary.com.]

are given in Tables II and III, respectively. The solidification temperature of HDPE is 377 K. The thermal property parameters of the air in the cavity are given in Table IV. It is worth mentioning that the parameter values in Table IV guarantee that the air is always in the gaseous state.

The fibers in the cavity are short glass fibers for the simulation in this paper, and each fiber is regarded as a short rigid rod with a slenderness ratio of 40. The density of fibers is 2.49×10^3 kg/m^3, and 200 fibers are distributed randomly in the initial melt, which is shown in Figure 12(a). A partial enlargement of

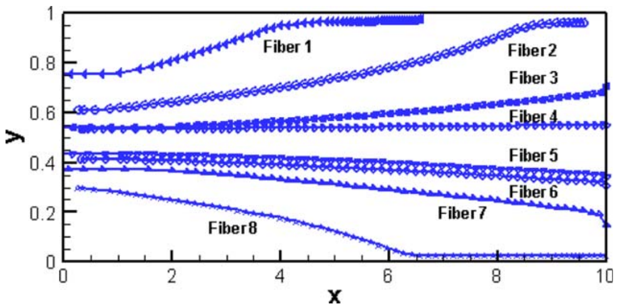

Figure 21. Single fiber trajectory in the cavity versus time. ($T_{\mathrm{wall}} = 303$ K, $T_{\mathrm{melt}} = 433$ K, $u = -4.0 \times (y - 0.5)^2 + 1, y \in [0,1]$, $t = 7546\ \Delta t$). (a) Distribution of pressure, (b) distribution of u velocity, (c) distribution of τ_{xx}, (d) distribution of τ_{yy}, (e) distribution of τ_{xy}, and (f) distribution of first normal stress difference. [Color figure can be viewed in the online issue, which is available at wileyonlinelibrary.com.]

the image within the square box is shown in Figure 12(b). In the mold-filling process, new fibers enter the cavity at each time step. Thus, new fibers must be generated randomly near the inlet at every time step. A total of 6000 fibers are generated during the mold-filling process in the simulation. For the flow field computation, Re = 0.01 and We = 0.01 and the inlet velocity $u = -4.0 \times (y - 0.5)^2 + 1$, $y \in [0,1]$.

"Frozen Skin" Layers

When cavity wall temperature $T_{\mathrm{wall}} = 303$ K, melt temperature $T_{\mathrm{melt}} = 433$ K, injection rate $u = -4.0 \times (y - 0.5)^2 + 1$, $y \in [0,1]$, $t = 7546\ \Delta t_{,}$ the temperature distribution in the cavity when the cavity is filled with melt is given in Figure 13, from which we see that the temperatures near the solid walls are very low. The temperature values decrease from the inlet to the end of the cavity. Figure 14 shows the frozen skin layer distribution (temperature distribution below the solidify temperature in the cavity) when the mold-filling process ends. A very thick frozen skin layer can be found near the solid walls of the cavity, especially at the end of the cavity. The frozen skin layers under different temperatures of melt and wall in the cavity and different injection velocities conditions were discussed in our previous work,[37] which showed that increasing the temperatures of the melt and the wall or increasing the injection velocity can efficiently eliminate the frozen skin layer.

Fountain Flow and Shear Rate Distribution

Figure 15 clearly shows the fountain flow effect at $t = 4000\ \Delta t$, that is, the polymer melt approaches the flow front from the center and diverts toward the wall.

Figure 16 shows the shear rate distribution at $x = 5$, $t = 7546\ \Delta t$. We can see that shear rate of the melt in the frozen skin layer near the wall is zero. Furthermore, the shear rate reaches the largest value near the subsurface of the cavity and very small in the middle of the cavity. This is in accordance with the finding reported by Yang *et al.*[30]

Fiber Dynamics

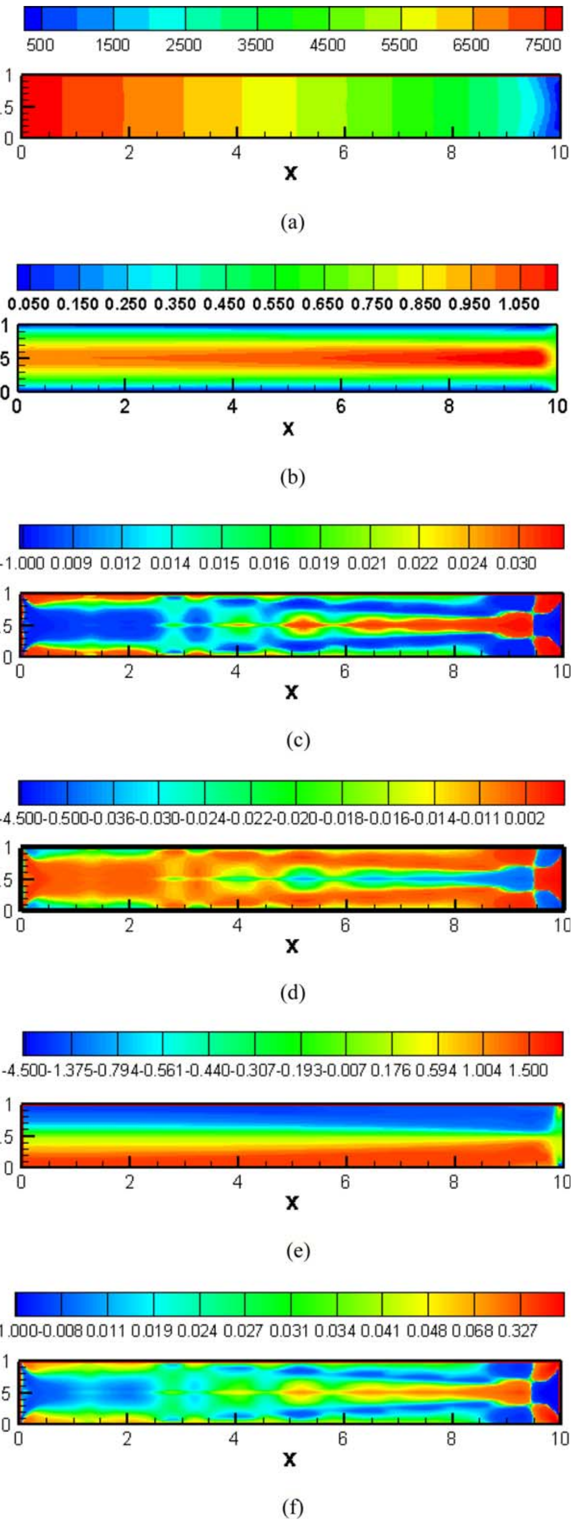

Figure 22. Physical quantities distribution in the cavity at the end of the mold-filling process. [Color figure can be viewed in the online issue, which is available at wileyonlinelibrary.com.]

Fiber Orientation. Figure 17 shows the translation and orientation of fibers with time in the cavity during the mold-filling process. Figure 18(a) shows a partial enlargement of Figure 17(e). In Figure 18(a), a skin-sub skin-core-sub skin-skin five-layer structure of the fibers orientation is observed. In the skin region, the fibers are distributed randomly, in the sub skin region, the fibers tend to align along the melt flow direction, while in the core region, the fibers are randomly oriented. The

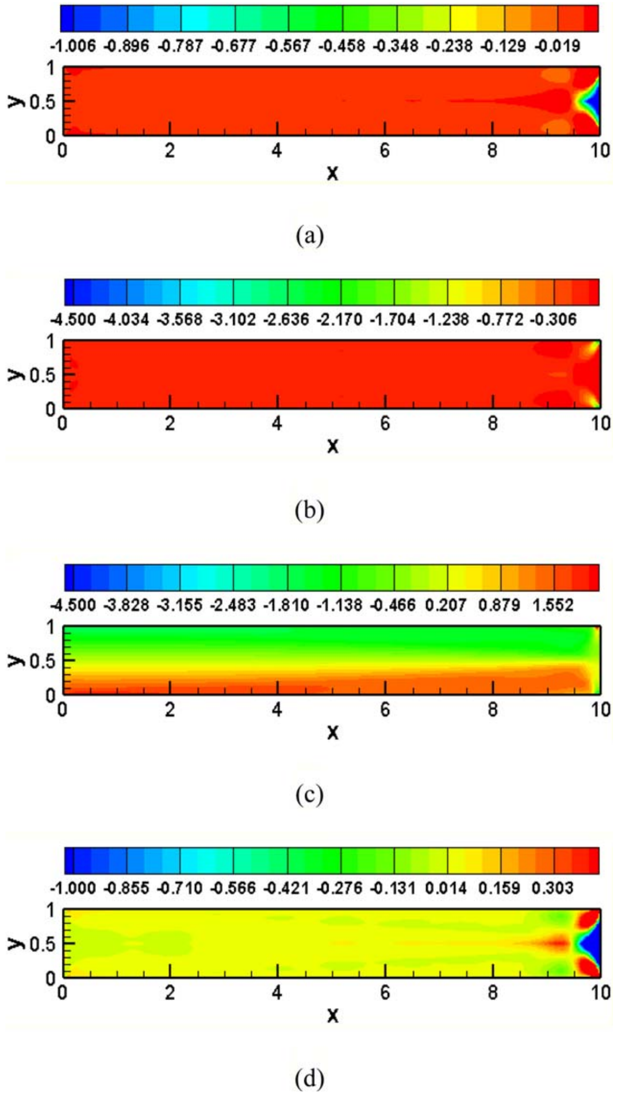

(a)

(b)

(c)

(d)

Figure 23. Stresses distribution in the cavity at the end of the mold-filling process without consideration of the influences of fibers and phase change ($T_{\text{wall}} = 303$ K, $T_{\text{melt}} = 433$ K, $u = -4.0 \times (y - 0.5)^2 + 1, y \in [0,1]$, $t = 7546\ \Delta t$). (a) Distribution of τ_{xx}, (b) distribution of τ_{yy}, (c) distribution of τ_{xy}, and (d) distribution of first normal stress difference. [Color figure can be viewed in the online issue, which is available at wileyonlinelibrary.com.]

reason for this alignment is that strong shearing takes place near the upper and lower side walls of the mold (subskin area), while the shear rate near the horizontal mid-line of the mold (core area) is low. At the same time, the temperature on the side walls of the mold cavity is much lower than that in the middle of the cavity, the polymer tends to solidify near the solid walls of the cavity, which is known as the phase change or frozen skin layer. Because there is no shear rate in the "frozen skin" layer, so fibers near the wall (skin area) are distributed randomly.

Figure 18(b) shows the translation and orientation of fibers at the end of the mold-filling process studied by Yang *et al.*[30] Comparing Figures 18(a) with 18(b), we can see that the fiber structures are not the same. The fibers are divided into three layers in Figure 18(b), and only a skin-core-skin structure of fibers exists within the rectangle box. However, the fibers are divided into five layers in Figure 18(a). This difference is a result of the phase change being ignored in Yang *et al.* simulation.[30]

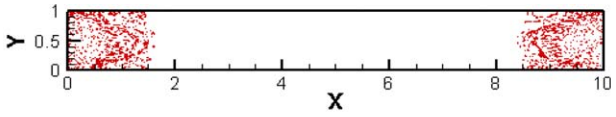

(a) $t = 200\ \Delta t$

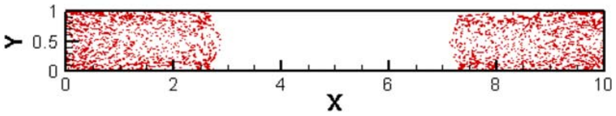

(b) $t = 400\ \Delta t$

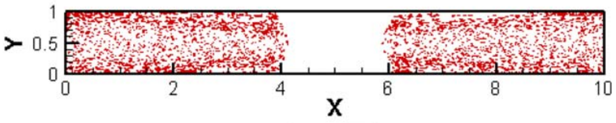

(c) $t = 600\ \Delta t$

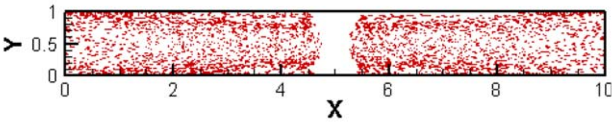

(d) $t = 700\ \Delta t$

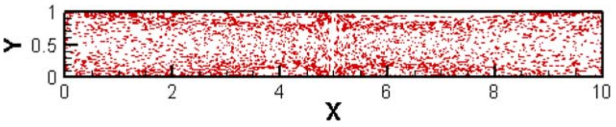

(e) $t = 745\ \Delta t$

Figure 24. Fiber motion in the cavity versus time. [Color figure can be viewed in the online issue, which is available at wileyonlinelibrary.com.]

Figure 19 is the experimental result of fiber orientation for fiber reinforced Polypropylene during mold-filling process in Liu *et al.*[57] In the experiment, short glass fibers with a length of 0.3mm and mass fraction 30% were taken. The mold temperature was 40°C, and the injection speed and injection time were 45 cm^3/s and 1.2 s, respectively. Figure 19(a) is the picture of fiber orientation, which is observed perpendicular to the direction of fluid flow in the cavity. Figure 19(b) gives fiber (near the cavity wall) orientation near the surface of the cavity, from which we see that the fibers orient randomly. Figure 19(c) gives fiber orientation near the subsurface of the cavity, from which we find that the fibers orient along fluid flow direction. Figure 19(d) is the fiber orientation in the middle of the cavity, from which we can see that the fibers orient randomly. Thus, it can be seen that the simulation results in this article is completely consistent to the experiment results of Liu *et al.*[57]

Influence of the Slenderness Ratio of the Fiber on Flow Field

Here is to discuss the disturbance influence of the slenderness ratio of the fibers on the physical quantities in the flow field. The fiber in melt is bound to have an impact on the velocity, stress and other physical quantities. The influence of the slenderness ratio of fibers on the maximum of velocity, pressure, stress and first normal stress difference are discussed in Figure 20. In Figure 20(a),

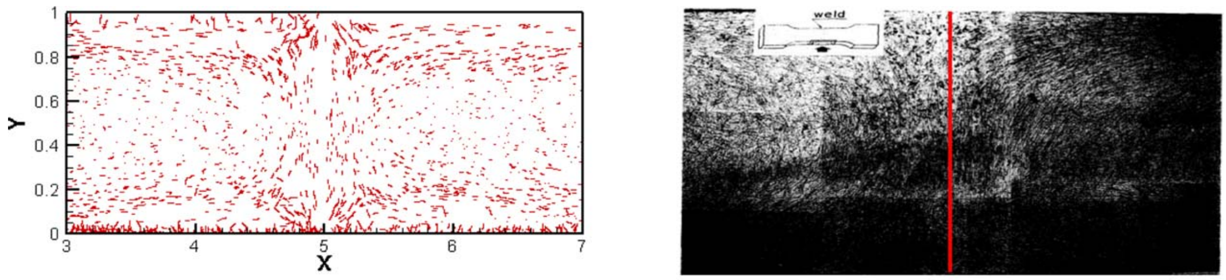

(a) (b)

Figure 25. The comparison of fiber orientation in weld line area between simulation result of this article and existing experimental results. (a) Simulation result of this article, (b) existing experimental results.[58] [Color figure can be viewed in the online issue, which is available at wileyonlinelibrary.com.]

the value of the velocity of melt without fibers is larger than that of melt with fibers. A bigger slenderness ratio of fibers has a stronger power to decrease the melt velocity. In Figure 20(b), the pressure in the cavity without fibers is smaller than that of melt with fibers. Figure 20(c–f) show that fibers orientation has disturbance on the stress and first normal stress difference. The influence is proportional to the slenderness ratio of the fibers. It is worth pointing out that the stress oscillates even without fibers in the melt. This may be caused by the phase change in the mold-filling process.

Single Fiber Trajectory in the Cavity

The motion trajectories of eight individual fibers in the cavity are shown in Figure 21. The initial coordinates of the eight fibers are (0.1297,0.7562), (0.2706, 0.6061), (0.1749,0.5381), (0.3167,0.5339), (0.1512,0.4348), (0.3258,0.4141), (0.0948,0.3713), and (0.2706, 0.3005), respectively. It can be seen from Figure 21 that the fibers near the upside and downside walls of the cavity move toward the upside and downside walls, respectively. This is because the motion of fibers is influenced by fountain flow effect as shown in Figure 15. The fibers near the middle of the cavity move nearly straight forward in a horizontal way.

Physical Quantities Distribution at the End of the Mold-Filling Process

Figure 22(a) shows the pressure distribution when the mold-filling process ends. ($T_{\text{wall}} = 303$ K, $T_{\text{melt}} = 433$ K, $u = -4.0 \times (y - 0.5)^2 + 1$, $y \in [0,1]$, $t = 7546\ \Delta t$). As can be seen in Figure 22(a), the pressure values decrease from the inlet to the end of the cavity, and the maximum pressure value is always located at the inlet. Figure 22(b) gives the distribution of u velocity, from which we can see that the u velocity decreases from the middle of the cavity to the side walls of the cavity. Due to the appearance of the frozen layer at the end of the cavity which makes the cavity tunnel narrower, the u velocity becomes larger when the melt passes through a narrower cavity tunnel. Figure 22(c–f) show the stress distributions when the mold-filling process ends, from which we can see that the distributions of τ_{xx}, τ_{xy}, τ_{yy} and the first normal stress difference are not smooth. This may be due to the phase change and the disturbance of fibers to stresses in the cavity. To show this, the stress values without the consideration of the influences of fibers and phase change are given in Figure 23. From the figures we can see clearly that the stress values without the consideration of fibers and phase change look smoother than those with the consideration of fibers and phase change.

Injection Mold-Filling Process with Double Inlets

Figure 24 shows the fiber motion versus time in the cavity with double inlets. It can be clearly seen from Figure 24 that the fibers on both sides in the cavity are still in the skin-sub skin-core-sub skin-skin structure until the cavity is filled with melt. In the injection molding process, when there are multigates, holes or insert in the cavity, the melt will flow along over two directions in the cavity, when the two melt meet, weld line will be formed in the product.

The partial enlargement of fiber orientation near the weld line in Figure 24(e) is shown in Figure 25(a). It can be seen that fiber orientation in the weld line area is perpendicular to the melt flow direction. On both sides of the weld line area, the fiber orientation is in the shape of semi arc, while away from the weld line area, the fiber orientation is still in skin-sub skin-core-sub skin-skin structure.

Fiber orientation near the weld line area was studied by experiment in Lim *et al.*[58] which is shown in Figure 25(b). In the experiment, short glass fibers of 0.3 mm and volume fraction 30% were mixed with the polycarbonate matrix. The melt temperature was 593 K and the cavity temperature is 388 K. As can be seen, the simulation results in this article are in qualitative agreement with experimental results in Lim *et al.*[58]

Convergence Test

Convergence analysis for the algorithm using three kinds of grid is shown in Table V. The code is run on a computer with CPU 2.8 GHz frequency, and 512 M memory. The profiles of velocity u, stress τ_{xy},τ_{yy} under different grids at $t = 8.0$, $x = 3$ are shown in Figure 26, which can validate the convergence of the algorithm.

Table V. Three Kinds of Grid for Convergence Validation

	Mesh	$\Delta x(\Delta y)$
Coarse	200 × 20	0.05
Intermediate	400 × 40	0.025
Fine	800 × 80	0.0125

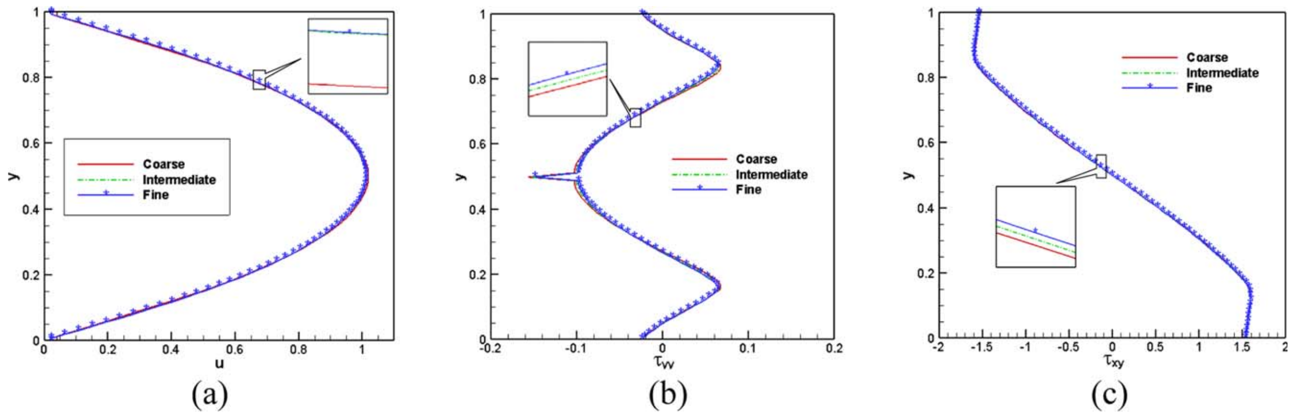

Figure 26. Convergence analysis for physical quantity under different grids ($t = 8.0$, $x = 3$). (a) Profiles diagram for u, (b) profiles diagram for τ_{yy}, and (c) profiles diagram for τ_{xy}. [Color figure can be viewed in the online issue, which is available at wileyonlinelibrary.com.]

CONCLUSIONS

In this article, a gas-solid-liquid three-phase model for the simulation of the mold-filling process for fiber-reinforced viscoelastic composites with phase change is established. A revised enthalpy method that can be used for both the melt and the air in the mold cavity is proposed to describe the phase change during the mold-filling. The interaction of the fibers and the polymer melt is considered in the model. A finite-volume method on a non-staggered grid with a momentum exchange source term is used to solve the viscoelastic-Newtonian fluid flow. The level set method is used to capture the front of the melt during the mold-filling process.

1. The frozen skin layers are simulated successfully. Information about the fiber transformation and orientation is obtained in the mold-filling process. A five-layered (skin-sub skin-core-sub skin-skin) distribution of fibers is found. In the skin region, the fibers are distributed randomly, in the sub skin region, the fibers tend to align along the melt flow direction, while in the core region, the fibers are randomly oriented, which is in accordance with previous experimental studies.
2. The influence of the slenderness ratio of fibers on the maximum of velocity, pressure, stress and first normal stress difference are discussed. Results show that fibers have disturbance on these physical quantities. The bigger the slenderness ratio, the larger the disturbance. At the same time, physical quantities such as velocity, pressure, temperature, and stresses distributions in the cavity at end of mold-filling process are also obtained.
3. The fiber motion versus time in the cavity with double inlets is simulated. It can be seen that fiber orientation in the weld line area is perpendicular to the melt flow direction. On both sides of the weld line area, the fiber orientation is in the shape of semi arc, while away from the weld line area, the fiber orientation is still in skin-sub skin-core-sub skin-skin structure. The results are in qualitative agreement with the experimental results.

The model we proposed in this article can capture the interface evolution and trace the trajectories of individual fibers. Most importantly, a dynamic mold-filling process can be obtained by our model. Since phase change during the mold-filling process is considered, the results that describe distribution of the physical quantities are more accurate than those ignoring the phase change.

ACKNOWLEDGMENTS

The authors would like to acknowledge the National Natural Science Foundation of Shanxi Province (2014011009-2), the Research Fund of Taiyuan University of Science and Technology (20112011), and the Outstanding Graduate Innovation Project of Shanxi Province (20133117).

REFERENCES

1. Wang, V. W.; Hieber, C. A.; Wang, K. K. *J. Polym. Eng.* **1986**, *7*, 21.
2. Chiang, H. H.; Hieber, C. A.; Wang, K. K. *Polym. Eng. Sci.* **1991**, *31*, 116.
3. Pichelin, E.; Coupez, T. *Comput. Method Appl. Mech. Eng.* **1998**, *163*, 359.
4. Smith, D. E.; Tortorelli, D. A.; Tucker, C. L. *Comput. Method Appl. Mech. Eng.* **1998**, *167*, 325.
5. Hetu, J. F.; Gao, D. M.; Garcia-Rejon, A.; Salloum, G. *Polym. Eng. Sci.* **1998**, *38*, 223.
6. Kabanemi, K. K.; Vaillancourt, H.; Wang, H.; Salloum, G. *Polym. Eng. Sci.* **1998**, *38*, 21.
7. Chang, R. Y.; Yang, W. H. *Int. J. Numer. Meth. Fluids* **2001**, *27*, 125.
8. Zhou, H. M.; Geng, T.; Li, D. Q. *J Reinf. Plast. Compos.* **2005**, *24*, 823.
9. Kim, S. W.; Turng, L. S. *Polym. Eng. Sci.* **2006**, *46*, 1263.
10. Zhou, J.; Turng, L. S. *Adv. Polym. Technol.* **2007**, *25*, 247.
11. Holm, E. J.; Langtangen, H. P. *Comput. Method Appl.* **1999**, *178*, 413.
12. Luoma, J. A.; Voller, V. R. *Appl. Math. Model.* **2000**, *24*, 575.
13. Khayat, R. E.; Elsin, W.; Kim, K. *Int. J. Numer. Meth. Fluids* **2000**, *33*, 847.

14. Ayad, R.; Rigolot, A. *J. Mech. Des.* **2002**, *124*, 813.
15. Kim, M. S.; Park, J. S.; Lee, W. I. *Int. J. Numer. Meth. Fluids* **2003**, *42*, 791.
16. Au, C. K. *Int. J. Mach. Tool. Manuf.* **2005**, *4545*, 115.
17. Geng, T.; Li, D. Q.; Zhou, H. M. *Eng. Comput. Ger.* **2006**, *21*, 289.
18. Soukane, S.; Trochu, F. *Compos. Sci. Technol.* **2006**, *66*, 1067.
19. Zhou, H. M.; Yan, B.; Zhang, Y. *J. Mater. Process. Tech.nol* **2008**, *204*, 475.
20. Yang, B. X.; Ouyang, J.; Liu, C. T.; Li, Q. *Chin. J. Chem. Eng.* **2010**, *18*, 600.
21. Khor, C. Y.; Ariff, Z. M.; Ani, C.; Abdul Mujeebu, F.; Abdullah, M.; Abdullah, M. K.; Joseph, M. Z. M. A. *Int. Commun. Heat Mass* **2010**, *37*, 131.
22. Yerramalli, C. S.; Waas, A. M. *CMES* **2004**, *6*, 1.
23. Brennan; Kelly, P. Walrath, David, E. *J. Thermoplast. Compos.* **2009**, *22*, 727.
24. Pyo, S. H.; Lee, H. K. *Cmes* **2009**, *40*, 271.
25. Zheng, R.; Kennedy, P.; Phan-Thien, N.; Fan, X. J. *J Non-Newtonian Fluid Mech.* **1999**, *84*, 159.
26. De Frahan, H.; Verleye, H.; Dupret, V.; Crochet, F. M. *J. Polym. Eng. Sci.* **1992**, *32*, 254.
27. McGrath, J. J.; Wille, J. M. *Compos. Sci. Technol.* **1995**, *53*, 133.
28. Kim, E. G.; Park, J. K.; Jo, S. H. *J. Mater. Process. Technol.* **2001**, *111*, 225.
29. Chung, D. H.; Kwon, T. H. *Korea-Aust. Rheol. J.* **2002**, *14*, 175.
30. Yang, B. X.; Ouyang, J.; Li, Q.; Zhao, Z. F.; Liu, C. T. *J Non-Newtonian Fluid Mech.* **2010**, *165*, 1275.
31. Sussman, M.; Fatemi, E.; Smereka, P.; Osher, S. *Comput. Fluids* **1998**, *27*, 663.
32. Sussman, M.; Fatemi, E. *SIAM J. Sci. Comput.* **1999**, *20*, 1165.
33. Osher, S.; Fedkiw, R. P. *J. Comput. Phys.* **2001**, *169*, 463.
34. Yang, B. X.; Ouyang, J. *Acta Phys. Sin* **2012**, *61*, 2346021.
35. Verbeeten, W. M. H.; Peters, G. W. M.; Baaijens, F. P. T. *J. Rheol.* **2001**, *45*, 823.
36. Aboubacar, M.; Aguayo, J. P.; Phillips, P. M.; Phillips, T. N.; Tamaddon-Jahromi, H. R.; Snigerev, B. A.; Webster, M. F. *J. Non-Newtonian Fluid Mech.* **2005**, *126*, 207.
37. Wang, F.; Li, J. L.; Yang, B. X.; Hill, N. A. *CMES* **2013**, *95*, 59.
38. Gupta, R. S.; Kumar, D. *A. Comput. Method Appl. Mech. Eng.* **1980**, *23*, 101.
39. Douglas, J.; Gallie, T. M.; Duke, *Math. J.* **1955**, *22*, 557.
40. Cao, Y.; Faghri, A.; Chang, W. S. *Int. Commun. Heat Mass* **1989**, *32*, 1289.
41. Kim, S. M.; Kim, C.; Chun, W. G. *Korean J. Chem. Eng.* **2001**, *18*, 40.
42. Caldwell, J.; Date, A. W. *Commun. Numer. Meth. Eng.* **2003**, *19*, 865.
43. Krabbenhoft, K.; Damkilde, L.; Nazem, M. *Int. Commun. Heat Mass* **2007**, *43*, 233.
44. Yang, B.; Fu, X. R.; Yang, W.; Huang, L.; Yang, M. B.; Feng, J. M. *Polym. Eng. Sci.* **2008**, *48*, 1707.
45. Cahn, J. W.; Hilliard, J. E. *J. Chem. Phys* **1958**, *28*, 1015.
46. Boronat, T.; Segui, V. J.; Peydro, M. A.; Reig, M. J. *J Mater. Process. Technol.* **2009**, *209*, 2735.
47. Yang, B. X.; Ouyang, J.; Jiang, T.; Liu, C. T. *CMES* **2010**, *63*, 191.
48. Tran-Cong, S.; Gay, M. E. *Powder Technol.* **2004**, *139*, 21.
49. Ouyang, J.; Li, J. H. *Chem. Eng. Sci.* **1999**, *54*, 2077.
50. Jeffery, G. B. *Proc. R. Soc. London Ser. A* **1922**, *102*, 161.
51. Zhou, K.; Lin, J. Z. *Fiber. Polym.* **2008**, *9*, 39.
52. Jiang, G. S.; Peng, D. P. *SIAM J. Sci. Comput.* **2000**, *21*, 2126.
53. Oliveira, P. J.; Pinho, F. T.; Pinto, G. A. *J. Non-Newtonian Fluid Mech.* **1998**, *79*, 1.
54. Osher, S.; Shu, C. W. *SIAM J. Numer. Anal.* **1991**, *2828*, 907.
55. Shu, C. W.; Osher, S. *J Comput. Phys.* **1989**, *83*, 32.
56. Shen, C. Y. Simulation of Injection Molding and Mold Optimization Design Theory and Method; Science Press: Beijing: **2009**; Chapter 8, pp 216–220.
57. Liu, B. C.; Shen, C. Y.; Liu, C. T.; Shangguan, L. J. *Eng. Plast. Appl.* **2009**, *37*, 52.
58. Lim, J. K.; Shoji, T. *KSME J.* **1993**, *7*, 173.